



The SHiP spectrometer magnet – Superconducting options

Hugues Bajas, Davide Tommasini

CERN

Abstract

This document describes a study of the choice of conductor and its design for the SHiP spectrometer.

The SHiP spectrometer magnet – Superconducting options

TABLE OF CONTENTS

1.	General introduction of the SHiP spectrometer magnet.....	4
1.1	Magnet dimensions	4
1.2	Magnet field request	4
1.3	Magnet total current	5
2.	Resistive magnet design	5
2.1	Magnet geometry	5
2.2	Conductor cross-section	6
2.3	Dissipated power	6
2.4	Mass of iron	7
3.	Superconducting magnet design	7
3.1	Introduction to the superconducting version.....	7
3.2	Description of the 3D model	11
3.3	Field error plot	18
3.4	Description of the 2D model	20
3.5	Magnet transfer function computation	24
3.6	NbTi option	25
3.7	Nb3Sn option	26
3.8	MgB2 option.....	27
3.9	ReBCO option.....	29
3.10	Superconducting option summary	30
4.	Conclusive remark	33
5.	Reference	34
6.	Annexe.....	35
6.1	Technical drawing for the resistive version	35
6.2	Coils geometry	36
6.3	Isometric views of the magnet	37
6.4	View of the 3D mesh	40
6.5	BH curve for the iron.....	41
6.6	View of the 2D mesh	42
6.7	Field lines, field in the acceptance region and in the iron for the 2D model.....	43
6.8	Magnet protection scheme	45
6.9	Critical surface scaling law	46
6.10	Material density.....	50
6.11	Conductor price	50
6.12	Summary tables for the superconducting options.....	51

1. General introduction of the SHiP spectrometer magnet

The spectrometer magnet for the Search for Hidden Particles (SHiP) experiment is a dipole magnet producing a horizontal dipole field within a window frame aperture of large dimension. The magnet is placed after a 40-m long decay volume that follows an upstream fixed target where particles from the CERN SPS accelerator interact [1], [2].

This report recalls the baseline magnet design, based on Aluminium hollow conductors, and explores different solutions of a superconducting version with coils made of either NbTi, Nb₃Sn, MgB₂ or ReBCO superconductors.

The main formulas for dipole magnet design used in this report comes from [2], [3], and the magnetic models are implemented in the Opera[®] software.

For each of the superconducting options, the critical surface parameterization come from available and well characterised strands. From the computation of the maximum field on the superconductor from model's data, the operating margins are derived, and the operating conditions defined in terms of temperature, peak field and current.

The strategy adopted for the protection of the magnet relies on external dump resistor as energy extraction system, and the superconductor itself is stabilized with enough copper to allow this operation in case of quench.

1.1 Magnet dimensions

The dimensions of the magnet for the spectrometer of the SHiP experiment are defined in [2]. The magnet's height h , width w and length l according to the technical drawing reported in the ANNEXE 6.1 are:

$$h = 13.8 \text{ [m]}$$

$$l = 7 \text{ [m]}$$

$$w = 7.28 \text{ [m]}$$

Also shown in the ANNEXE 6.1, the limit of acceptance enclosed by the poles is a free rectangular surface of 5000x10000 mm.

1.2 Magnet field request

The magnet shall provide a vertical bending strength of 0.65 Tm going from -2.5 to +2.5 m along the magnetic axis and with respect to the magnet centre. The request for the central field B_0 is 0.15 T. The field is produced by bedstead shaped coils assembled in a dipole field configuration around and iron core.

The maximum field induction in the iron yoke is $B_{iron,max}=1.76$ T at the nominal bending strength as defined in [1]. The thickness of the iron yoke along coil axis is 3.5 m [1]. Following the recommendation from [2], the iron yoke is an assembly of 70 layers, each 50 mm thick.

1.3 Magnet total current

In order to achieve the required bore field B_0 within the given aperture (*gap*) analytical formula for a dipole magnet [3] gives the magnet total current NI_{total} as function of the bore field and the magnet efficiency η :

$$NI_{total} = \frac{B_0 * gap}{\eta * \mu_0} = \frac{0.15 * 5.4}{0.9 * 4\pi * 10^{-7}} = 720000 \text{ [A. turn]}$$

2. Resistive magnet design

The magnet design, for its resistive version, features three coil packs per pole with each pack hosting four pancakes of array of 10 conductors [2]. The conductor is made of hollow aluminium similar to the one used for LHCb.

2.1 Magnet geometry

Fig. 1 shows the Opera® model of the magnet featuring the three coils per pole (red color) surrounded by the iron yoke (green color) [4].

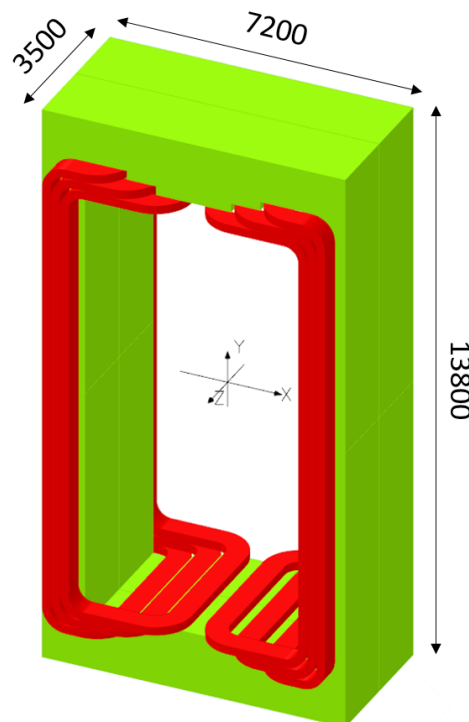


Fig. 1 : Global view of the Opera® 3D model for the resistive version of the SHiP spectrometer. It features in green color the iron yoke and in red the coils (three coils per pole).

Fig. 36 in Annexe 6.2 gives the details of the coil geometry for the six coils.

2.2 Conductor cross-section

The cross-section of a coil with the 40-conductor array is shown in Fig.2. The conductor is similar to the one used for the LHCb magnet (Al-99.7) with a 50x50 mm² square cross-section with a 25-mm diameter central bore hole for water cooling made of Aluminium. A composite layer (glass fiber and resin) 2 mm thick provides the dielectric insulation between turns.

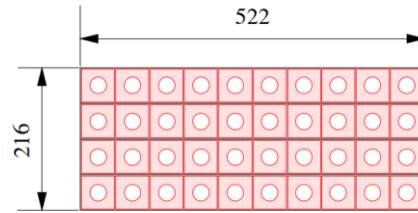


Fig. 2 : SHiP spectrometer coil's cross-section of the resistive (Aluminium) hollow conductors array .

With N_{pole} the number of poles, N_{coil} the number of coils per pole and N_{turn} the number of turns per coil, the magnet's total number of turns N_{total} is:

$$N_{total} = N_{pole} * N_{coil} * N_{turn} = 2 * 3 * 40 = 240 [-]$$

Dividing the total magnet current by the total number of turns gives the current per conductor:

$$I_{cond} = \frac{I_{total}}{N_{total}} = \frac{720000}{240} = 3000 \text{ [A]}$$

The cross-section area of one conductor is:

$$A_{cond} = 50^2 - \pi * \frac{25^2}{4} = 2009 \text{ [mm}^2\text{]}$$

The conductor's current density is then:

$$j_{cond} = \frac{I_{cond}}{A_{cond}} = \frac{3000}{2009} = 1.49 \text{ [A/mm}^2\text{]}$$

Using this magnet geometry and coil design, the report in [4] gives a field in the centre of the magnet's aperture B_0 of 0.154 T in agreement with theoretical value.

2.3 Dissipated power

The developed length of conductor per coil from in Fig. 36 of Annexe 6.2 is:

$$l_{cond} = 37.2 \text{ [m]}$$

With a conductor resistivity $\rho_{e,cond}$, the magnet's total power consumption is:

$$\begin{aligned} P_{total} &= \rho_{e,cond} * j_{cond}^2 * A_{cond} * l_{cond} * N_{total} \\ &= 2.8 * 10^{-8} * (1.49 * 10^6)^2 * 2009 * 10^{-6} * 37.2 * 240 = 1.11 \text{ [MW]} \end{aligned}$$

Using forced convection water cooling solution, with a Reynolds number of 53400, that corresponds to a total flow of 1080 l/min, the water temperature increases by 15.4 K [4].

2.4 Mass of iron

The yoke is a stack of 70 iron layers 50 mm thick. The width of the vertical and horizontal parts of the yoke layers being 1 and 1.5 m, the lamination weight is estimated:

$$Mass_{yoke} = \delta_{iron} * N_{layer} * A_{iron} * w_{iron,layer} = 7900 * 70 * 2 * ((7.2 - 1) + (13.8 - 1.5)) * 0.05 = 1023 \text{ tons}$$

3. Superconducting magnet design

3.1 Introduction to the superconducting version

The objective of the study is to explore an alternative to the resistive version with a design of superconducting magnet that is competitive in terms of power consumption and material cost.

3.1.1 Superconducting options

We consider four different superconductors working at four different temperature ranges as a case study:

- the NbTi LHC main dipole strand (LHC MB inner layer) at 6 K, [5], [6], [7].
- the Nb₃Sn HL-LHC QXF strand from OST at 15 K [8].
- the MgB₂ strand from the HL-LHC superconducting link [9] or the flat MRI conductor from Columbus Superconductor at 20 K [10].
- the ReBCO conductor from Fujikura at 50 K [11].

Since the superconducting properties of these materials strongly depends on the applied field, one must precisely assess its maximum amplitude at the level of the conductor. The peak field is computed with Opera[®] software 2D and 3D simulations.

3.1.2 Superconducting coil design

For the superconducting version, the magnet is also made of six coils (three per pole) and an iron yoke. Each coil is a double pancake that hosts a winding made of two layers of one single-copper-stabilized-superconducting-wire.

According to the superconductor type, the number of turns and the level of current is adapted to produce the required field induction. The coils position is such they cover the aperture width and keep good field homogeneity near the iron. The coils dimensions are kept as short as possible to save conductor cost.

3.1.3 Operating conditions

From the numerical model, one computes the magnet load line as the maximum field at the conductor's level as function of the conductor current. Together with the critical surface of the superconductor, one determines the operating margin in terms of quench field as:

$$Margin = 100 * \frac{B_{ss} - B_{cond}}{B_{ss}}$$

Where B_{ss} is the short sample field (intersection of the load line with the critical surface) and B_{cond} is the field computed on the conductor at nominal current.

For each superconducting option, the goal is to find out the most relevant operating temperature keeping the margin on quench field above 30%.

3.1.4 Magnet protection

One issue dealing with superconducting coils is their protection during a quench. In all cases we allow a maximum hot spot temperature to increase up to 50 K during a quench.

The superconducting material is stabilized with copper layers bound to the superconductor and an external dump resistor is used as energy extraction system.

A voltage detection system is required for superconducting magnet and necessarily implied the positioning of voltage taps distributed along the coil winding [13].

3.1.4.1 Copper stabilized superconductor

An adiabatic thermal model of the stabilized superconductor gives the relation between the current density in the copper stabilizer $J_{Cu,max}$ and the Hot Spot temperature [14]. With I_{op} the operating current, the total copper area $S_{Cu,total}$ reads:

$$S_{Cu,total} = \frac{I_{op}}{J_{Cu,max}}$$

The area of the stabiliser is then:

$$S_{Cu,stab} = S_{Cu,total} - S_{Cu,strand}$$

Taking a rectangular cross-section for the copper stabilizer around the conductor with an aspect ratio of 3, both sides a and b of the rectangle get sizes as:

$$a = \sqrt{\frac{S_{Cu,stab}}{3}}$$

$$b = 3 * a$$

With the density of copper of ρ_{Cu} , the density of the superconductor ρ_{Sc} , the copper-to-non-copper ratio α_{Cu-nCu} and the total conductor length l_{cond} , the superconductor's weight m_{Sc} and the copper stabilizer's weight $m_{Cu,stab}$ read:

$$m_{Sc} = \frac{l_{cond} * A_{strand}}{\alpha_{Cu-nCu} + 1} * (\alpha_{Cu-nCu} * \rho_{Cu} + \rho_{Sc})$$

$$m_{Cu,stab} = \rho_{Cu} * l_{cond} * S_{Cu,stab}$$

3.1.4.2 Protection scheme

The following part gives the main parameters relative to the magnet protection RL circuit. Such circuit is given in the ANNEXE Fig. 48.

1. Magnet inductance

The magnet inductance is computed from the 3D Opera® model using the integral of the field over the whole volume. From the stored energy,

$$E_{st} = \iiint \frac{B \cdot H}{2} dV$$

The magnet's inductance can be obtained [3]:

$$L_{total} = \frac{2E_{st}}{I_{total}^2}$$

2. Maximum allowable voltage

The value for the resistance of the external dump is set according to the maximum allowable voltage U_{max} . By design, we set:

$$U_{max} = 1000 \text{ [V]}$$

3. Dump resistance

According to the quench current and the maximum voltage, the dump resistor value reads:

$$R_{dump} = \frac{U_{max}}{I_{op}}$$

4. Extraction time constant

Neglecting the magnet resistance, the time constant during the extraction corresponding to an exponential decay of the current is:

$$\tau = \frac{L_{total}}{R_{dump}}$$

5. Quench integral

The quench integral for an exponential decay reads:

$$QI = 0.5 * \tau * I^2$$

The quench integral must be sufficiently low to maintain the conductor temperature below a maximum allowable temperature T_{MAX} of 50 K.

6. Hot Spot Temperature assessment

An example of temperature increase as function of the quench integral is shown in Fig.3. It displays two cases, where the current is either 200 A and 500 A, the magnet inductance, either 230 H or 37 H, the dump resistor either 5 Ω or 2 Ω. For both cases, the copper stabilizer cross-section is of 17.5 mm². Both cases start either a 20 and 8 K. Adiabatic assumption is made for this computation taking into account the non-linear dependence of the copper resistivity and Volumetric Heat Capacity [14].

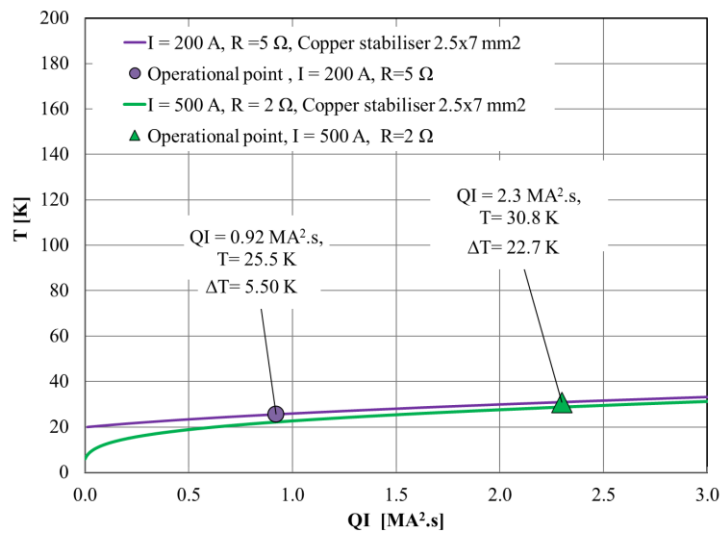


Fig. 3: Example of temperature increase in the coils following a quench.

Fig. 4 shows the dependence of the temperature variation as function of the copper stabilizer amount for the low and high current cases. This curve is used to dimension the amount of copper needed to protect the conductor.

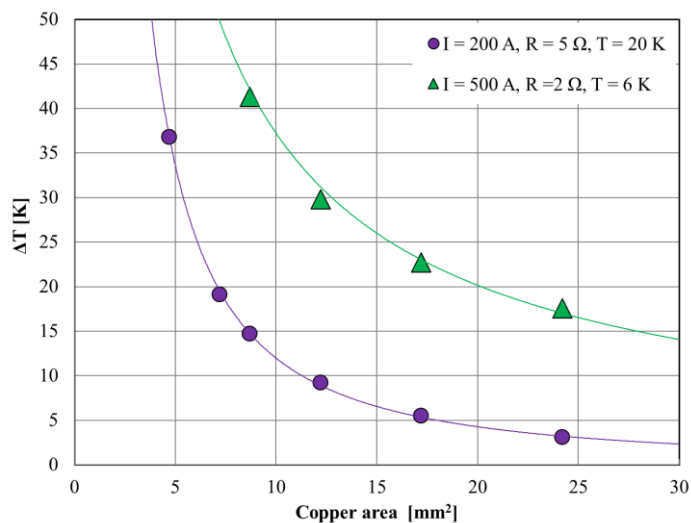


Fig. 4 : Dependence of the temperature variation as function of copper stabilizer amount.

3.2 Description of the 3D model

3.2.1 Geometry

Fig. 5 shows the 3D model built with Opera® 3D software for the superconducting version of the SHiP spectrometer. The model includes the air region, the iron yoke and the coils. The air region is a parallelepiped with the following dimensions: 5400x8800x10000 mm³ sufficiently large not to influence the field within the magnet.

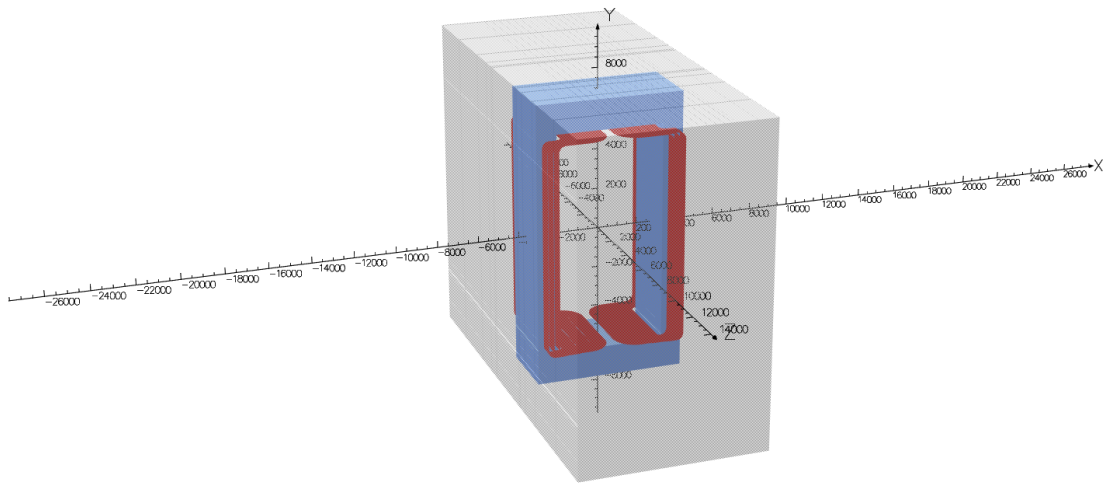


Fig. 5 : Global view of the Opera® 3D model for the superconducting version of the SHiP spectrometer. In grey color the air region, in blue the iron yoke and in red the conductors.

Annexe 6.3 shows the isometric views of the magnet with the various dimension.

3.2.2 Boundary conditions

The symmetries of the system allow modelling one eighth of the full magnet applying either normal or tangential field boundary conditions at the symmetry planes.

Fig. 6 shows the reduced model and the boundary conditions applied to these external surfaces.

Normal field boundary condition applies on the symmetry plane YZ at X=0.

Tangential field boundary condition applies on both symmetry planes XZ at Y=0 and XY at Z=0 and on the three far field faces of the model.

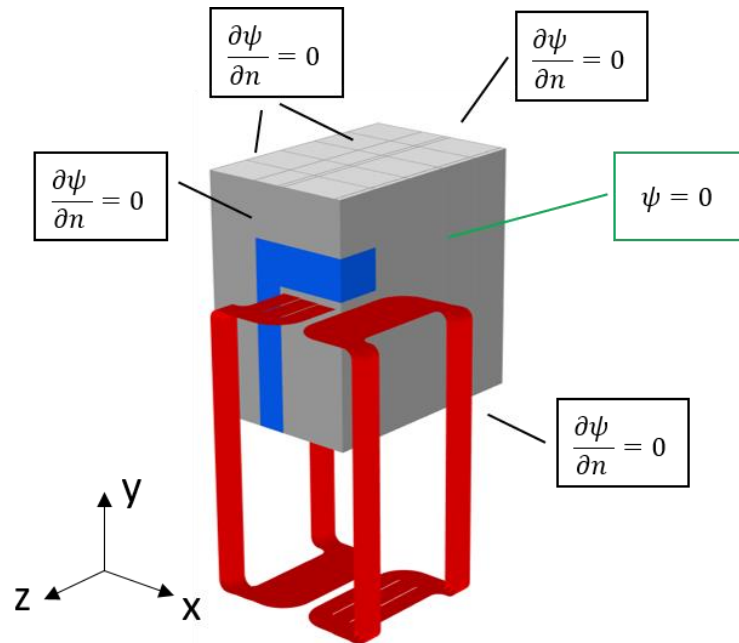


Fig. 6 : View of the reduced symmetric model (one eighth of the full model) with Dirichlet and Neumann boundary conditions applied on the external faces. ψ is the magnetic scalar potential (null for normal field condition) and $\frac{\partial\psi}{\partial n}$ its normal derivative (null for tangential field condition).

3.2.3 Controlled mesh

The mesh size is the crucial ingredient of the model. The conductor thickness is much smaller than the other dimensions of the magnet. To precisely describe the magnetic behaviour at the level of the conductor needed to determine the coil peak field, the mesh density should be much higher at the conductor vicinity. The total number of elements is 3332160. This degree of mesh refinement is the only way to get precise coil field integration results.

Annexe 6.4 shows the views of the mesh for the isometric views.

3.2.4 Material properties

Annexe 41 shows the non-linear BH curve used for the iron magnetic properties of the iron core.

3.2.5 Field in the iron

Fig. 7 shows the field map on the iron with a maximum value of 1.53 T at the corner of the yoke. The design respects the constraint of having a field below 1.75 T in the iron.

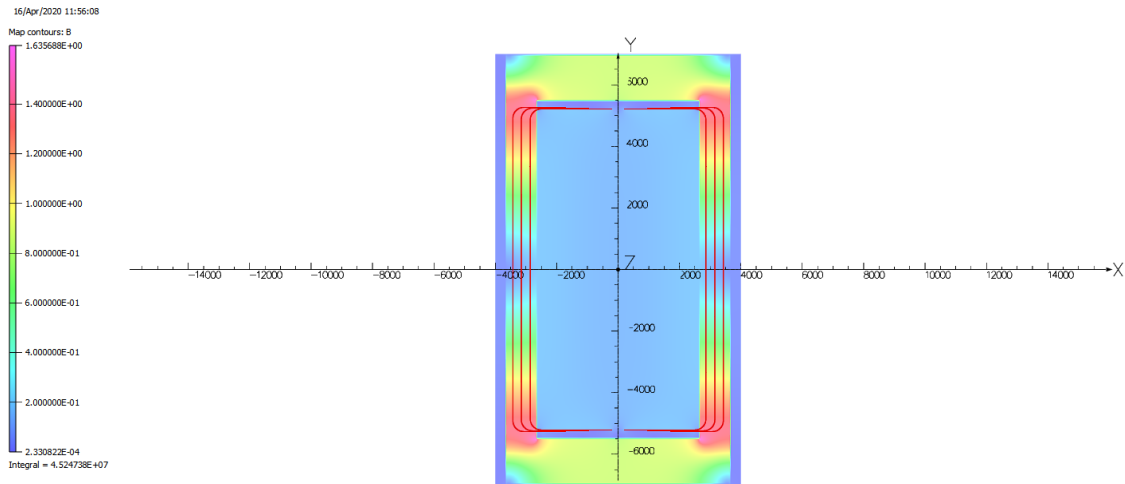
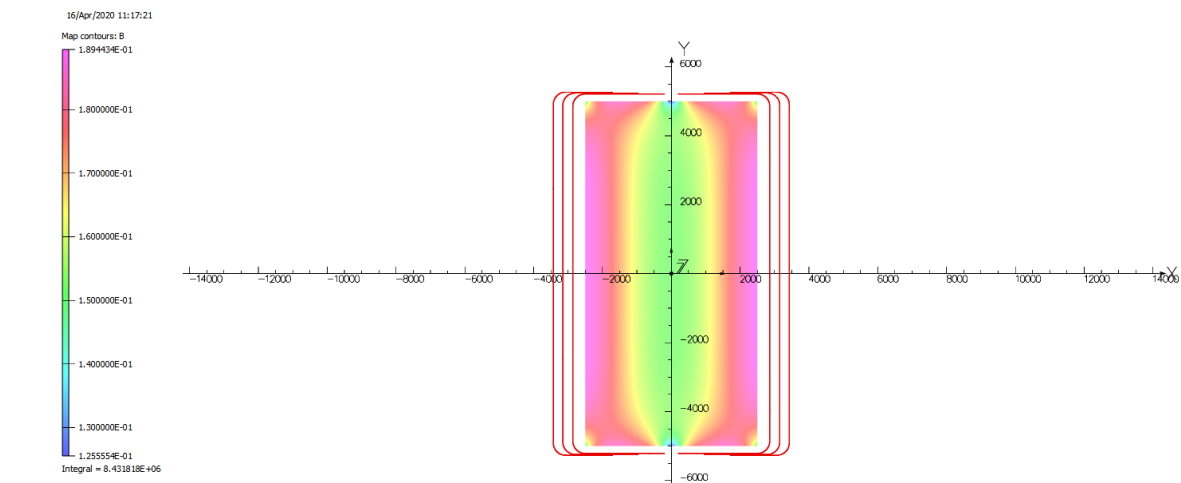


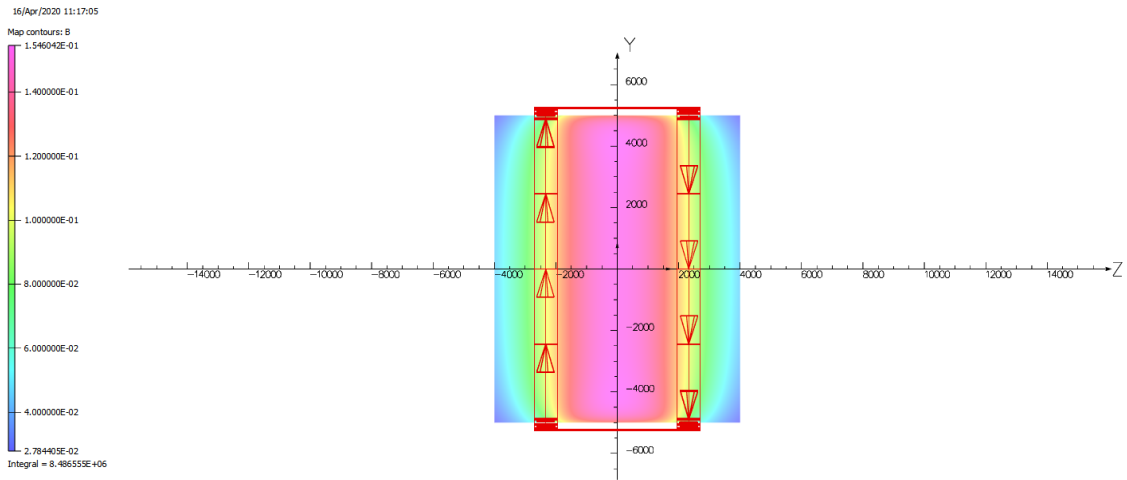
Fig. 7 : Field map on the iron yoke measured on the XY plane at Z=0.

3.2.6 Field in the beam acceptance region

Fig. 8 a) and b) shows the field map calculated within the acceptance limit (at Z=0) respectively along the XY and ZY planes. The field at the origin B_0 is 0.153 T, the maximum field is B_{max} is 0.189 T below the conductor.



a)



b)

Fig. 8: Magnetic field map on the acceptance limit rectangle with a) on the YX and b) YZ plans.

Fig. 9, Fig. 10 and Fig. 11 show the field along respectively the X, Y and Z-axis at various locations within the acceptance limit. The plots allow appreciating the field distortion near the conductor or near the iron yoke as well as the field uniformity with the acceptance limit.

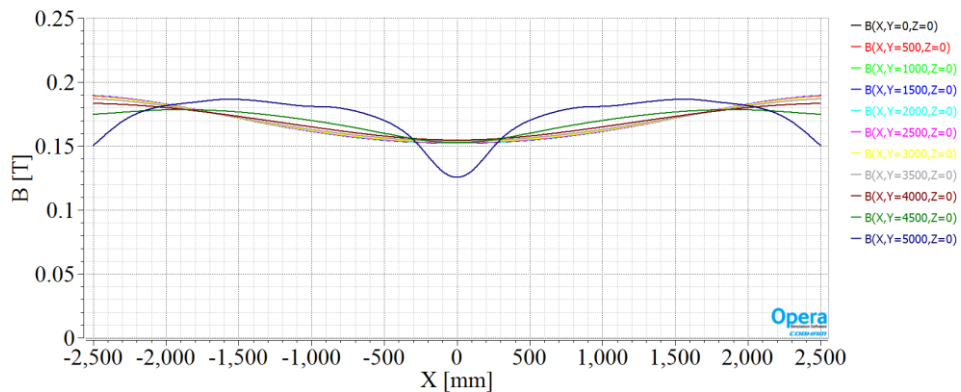


Fig. 9: Field along the X-axis at different Y altitudes and at Z=0.

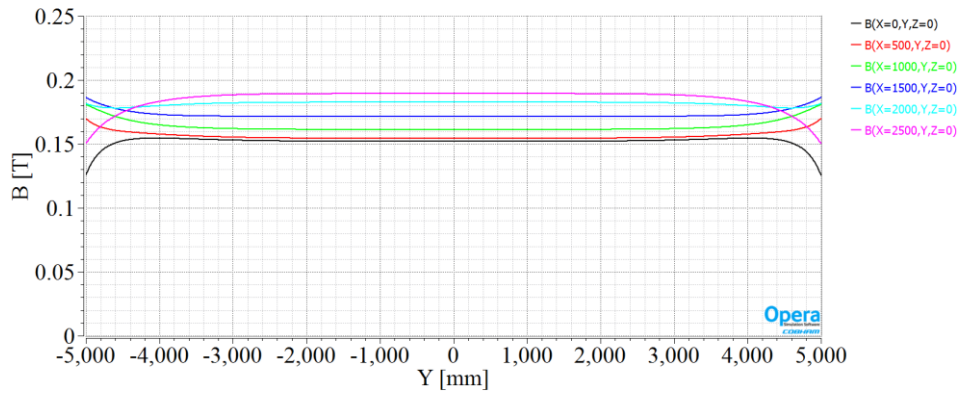


Fig. 10: Field along the Y-axis at different X locations and at Z=0.

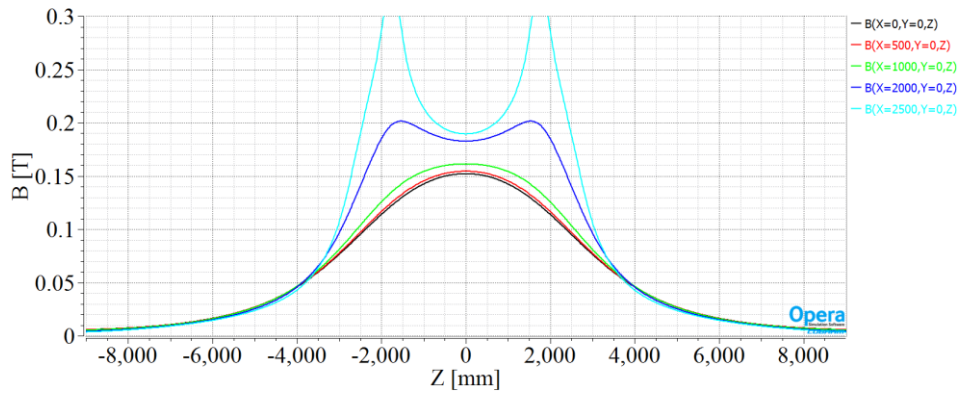


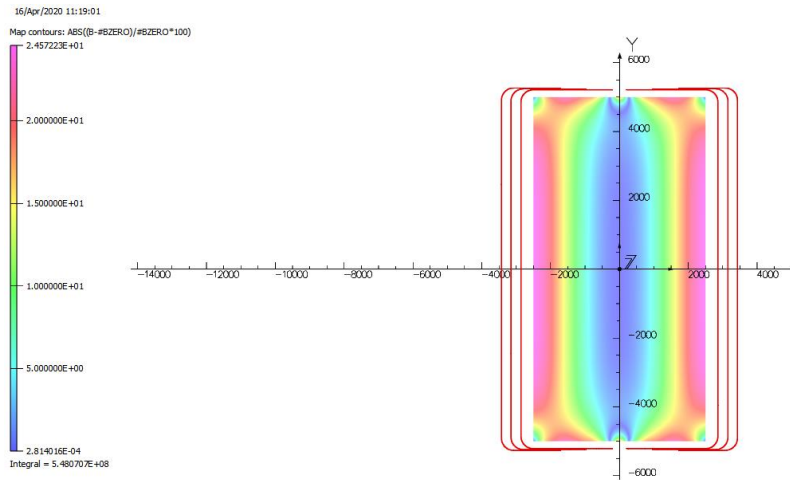
Fig. 11: Field along Z-axis at different X locations and at Y=0.

3.2.7 Field homogeneity in the beam acceptance region

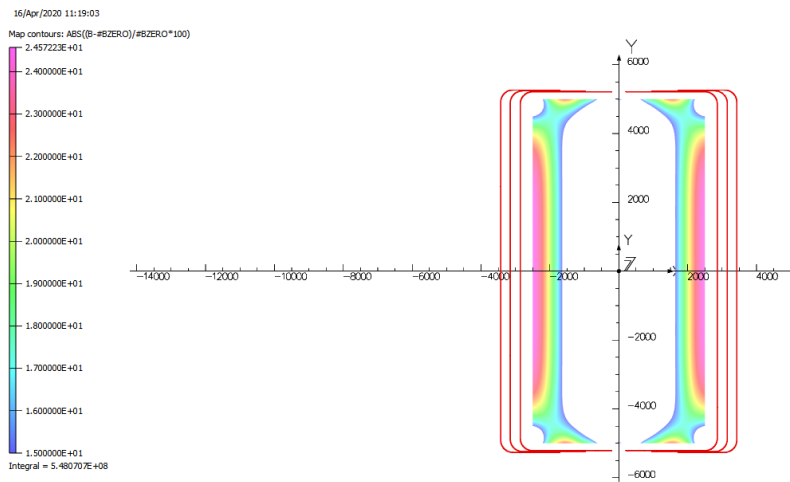
Fig. 12 shows the field map error, representative of the field homogeneity, within the acceptance limit. The definition of the field error expressed in percent is:

$$Error\ B = 100 * \left(\frac{B - B_0}{B_0} \right)$$

Where B_0 is the field at the origin that is 0.153 T.



a)



b)

Fig. 12: a) Magnetic field homogeneity map within the acceptance limit (XY plan).
b) Same map removing the zone where the error is below 15%.

Fig. 13 shows the field error map in the YZ planes. The error is mostly below 5 % and increases in the zone close to the conductor or near the iron yoke. The field quality matches the need of the physics of the detector in terms of field homogeneity.

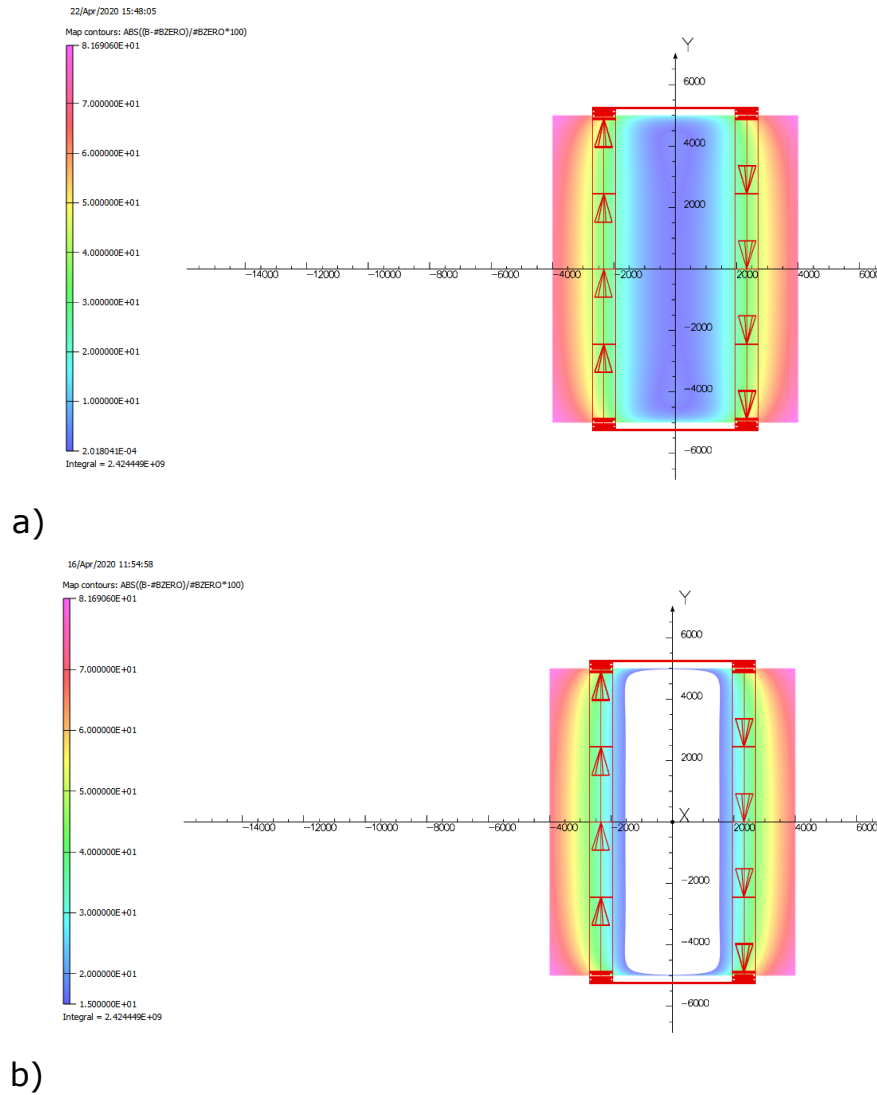


Fig. 13: a) Magnetic field homogeneity map within the acceptance limit (YZ plan).
b) Same map removing the zone where the error is below 15%.

3.3 Field error plot

Fig. 14, Fig. 15 and Fig. 16 show the plots of the error along the three directions computed for different locations.

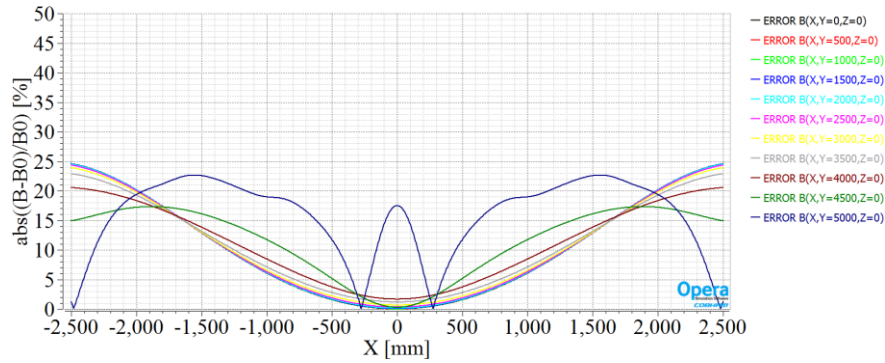


Fig. 14: Field error along the X-axis measured at different altitudes Y at Z=0.

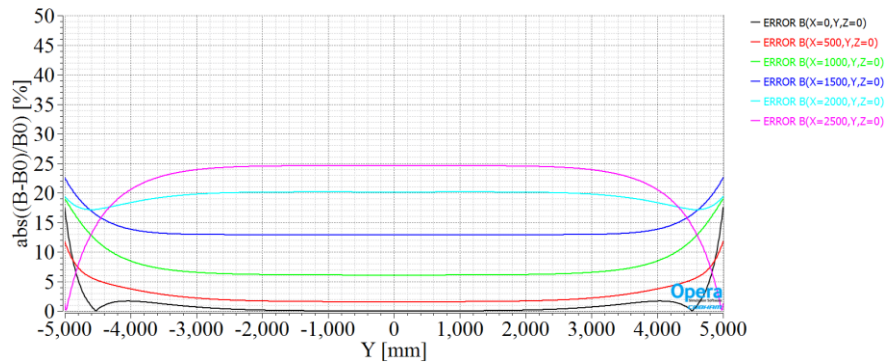


Fig. 15 : Field error along the Y-axis measured at different position along X at Z=0.

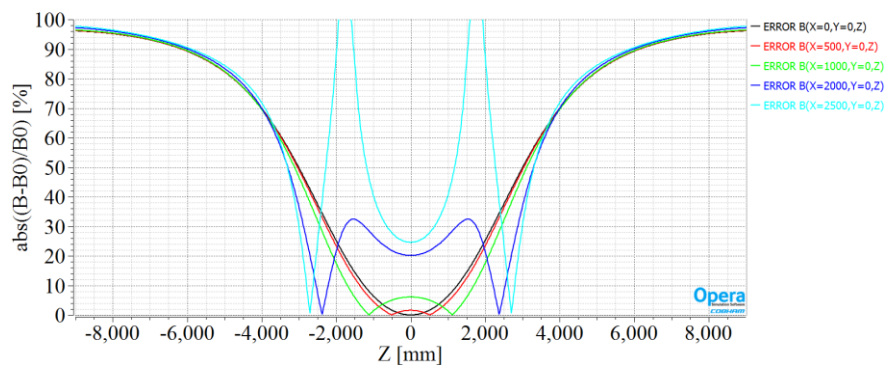


Fig. 16 : Field error along the Z-axis measured at different positions along X at Y=0.

3.3.1 Field on the superconductor

The field applied on the conductor needs to be precisely determined in order to derive the magnet load line. Opera offers two methods for the coil field determination: the nodal interpolation and the integration method. The first method is straightforward but gives less accurate results compared to the second that requires an extra step of computation. Both methods request very fine mesh along and across the coil to get coil field results converging.

Fig. 17 shows the coil's field map computed using the integration method. The maximum value B_{peak} reads 0.453 T. The field concentrates in the inner coil at the corner near the iron.

For the integration method, the numerical parameter called *MAXEDGEHDLPTS* (the maximum number of additional field points) must be increased up to its maximum value of 1082. The nodal interpolation considering the extremely thin dimension of the coil with respect to the finite element mesh is less accurate than the integration method.

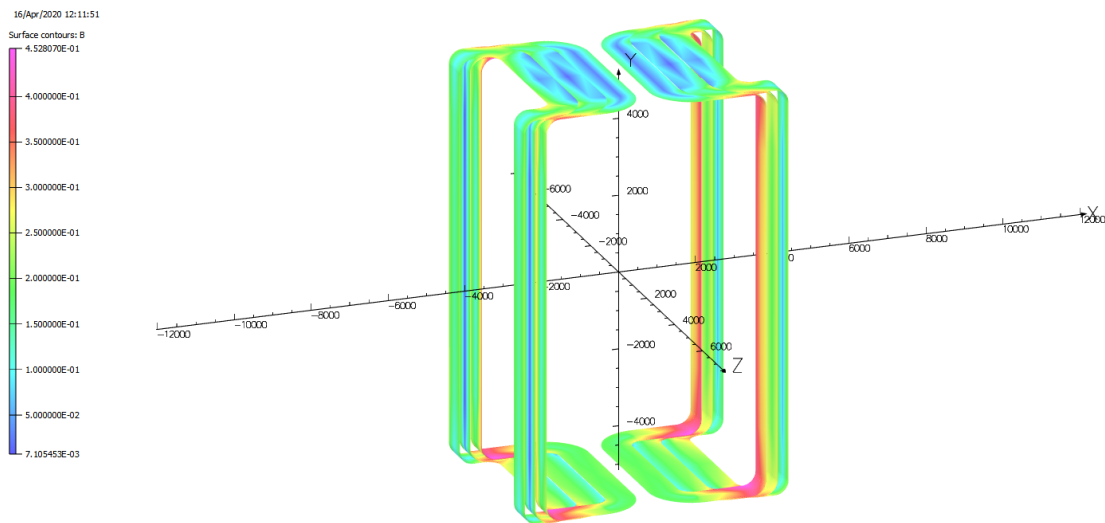


Fig. 17 : Field on the coil computed using the integration method.

In order to confirm the validity of the coil field computation, a 2D model of the magnet has been built that allows to describe more precisely the magnetic field within the conductor cross-section than what can be obtained with the 3D model.

3.4 Description of the 2D model

3.4.1 Geometry and boundary conditions

Fig. 18 shows the global view of the 2D model built using Opera® 2D software with the conductor layer, the iron, and the air region. The 2D model corresponds to the mid plane of 3D model, saying the plane XY at Z=0 and keeps the same dimensions for the iron yoke and the conductor. For symmetry reason only one fourth of the system is modelled applying normal and tangential boundary conditions.

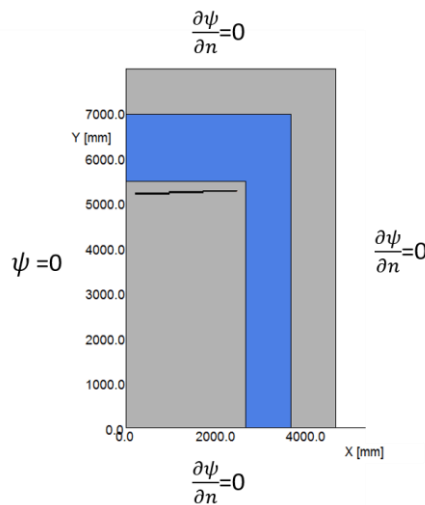


Fig. 18: Global view of the 2D Opera® model featuring in grey color the air region, in blue color the iron yoke and in red the conductor. Boundary conditions indicated for each external side.

The smeared region corresponds to the conductor geometry as used in the 3D model. The detailed regions represent individual turns and allow evaluating the field enhancement due to the local concentration of the current density.

Fig. 19 a) shows the conductor geometry with the copper stabilizer sandwiching the superconducting material. The coil pack features the three-double-layer (A and B) coils (1, 2 and 3). Both a detailed and smeared region divide the conductor.

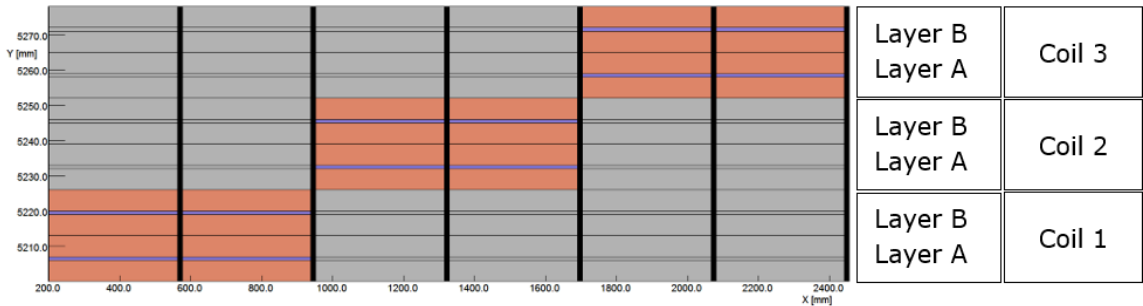
Fig. 19 b) shows the zoom-in the detailed region where each superconducting cell is a square of $1 \times 1 \text{ mm}^2$ area. The copper thickness separating the turns is 0.75 mm on each side of the superconducting cell and the thickness separating the layer is and 6 mm. The width of one coil is then:

$$w_{coil} = 300 * (1 + 2 * 0.75) = 750 \text{ mm}$$

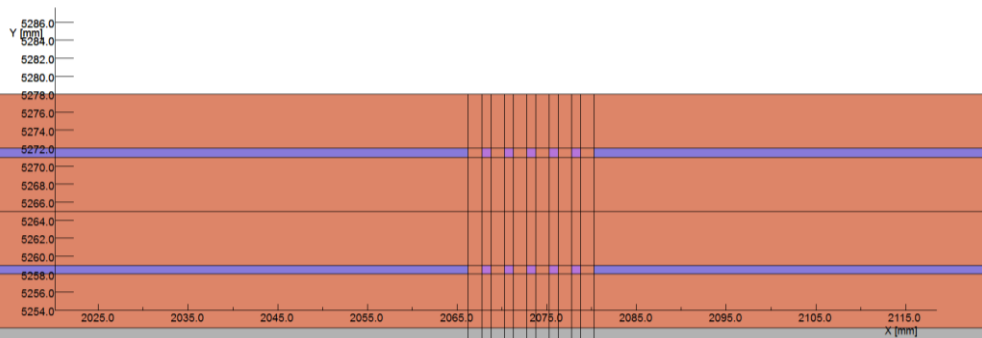
In this simplified model, the intern turn insulation is encompassed in the 0.75 mm.

Opera® 2D limits the number of regions to 5000 so it is not possible to model thousands of turns (each turn contains 6 regions). For that reason, only some

parts of the conductor get a refined geometry (at the edges and at the centre of the coils).



a)



b)

Fig. 19: a) View of the conductors with three coils made of two 1-mm thick layers of superconductor (violet color) sandwiched between two 6-mm thick copper sheet (orange color). b) Zoom-in the refined geometry of the coil 3 showing the separated turns with 5 superconducting cells between two smeared regions.

3.4.2 Controlled mesh

Just as for the 3D model, the quality of the mesh for the 2D model is of prior importance. The 2D mesh can be refined at the conductor level to a much higher degrees of precision with respect to the 3D model.

Annexe 0 shows the mesh used for the 2D model.

3.4.3 Current density in the superconductor

Fig. 20 shows the current density within the superconducting material for the detailed zone (200 A/mm^2) and smeared zone (80 A/mm^2). One can check that the integral of the current over the superconducting area is well equal to the total current ($360\,000 \text{ A.turn}$).

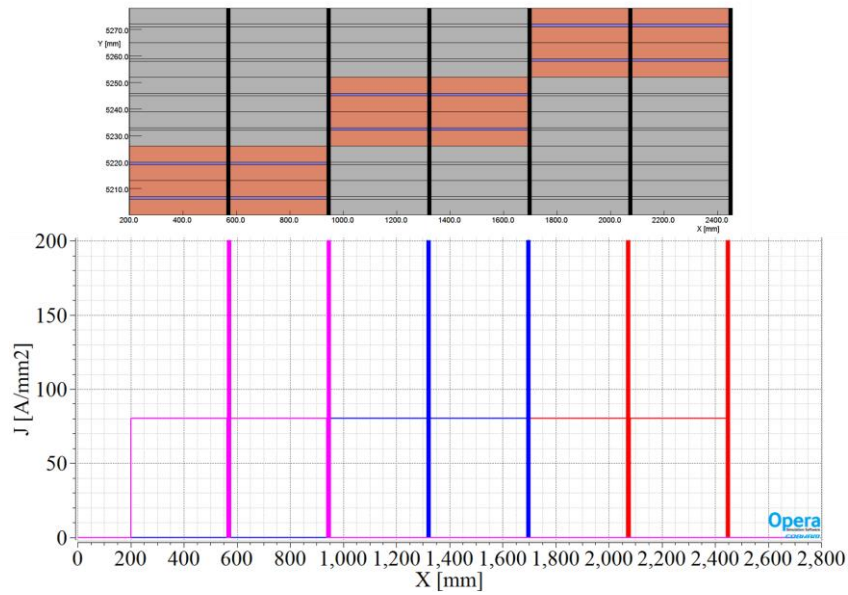


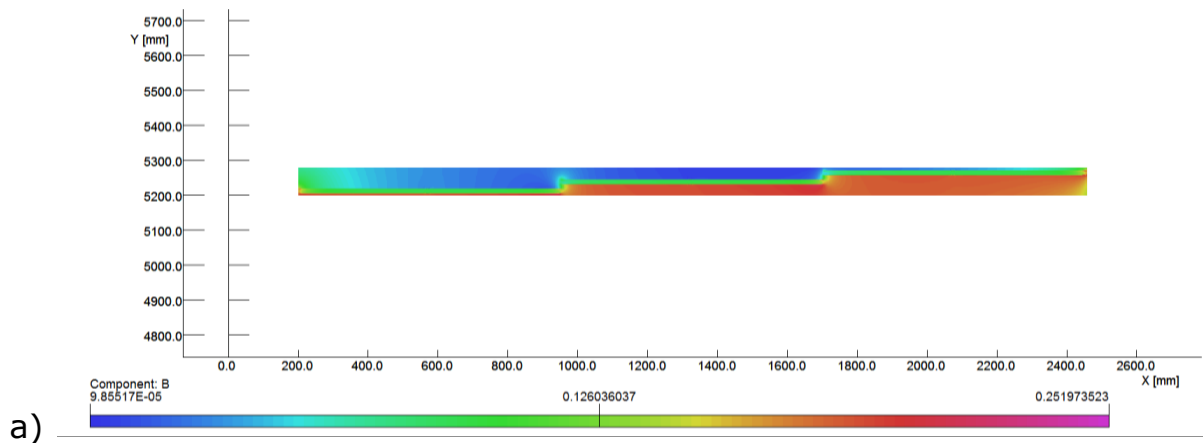
Fig. 20: Plot of the current density across the conductor. The insert above the plot shows the conductor geometry.

3.4.4 Intermediate result checking

The results of the 2D computation in terms of field lines, field in the acceptance region and in the iron are reported in Annexe 0.

3.4.5 Field on the superconductor

Fig. 21 a) shows the field map of the conductor region with a maximum field of 0.25 T. Fig. 21 b), c) are two zoom-in views from two locations at the interface of the coil 1 and 2 and coil 32 and 3. Fig. 21 d) is a zoom-in the last turn of the last coil showing the importance of modelling the separated turns to accurately describe the local magnetic field. Of the field map measured on the conductor.



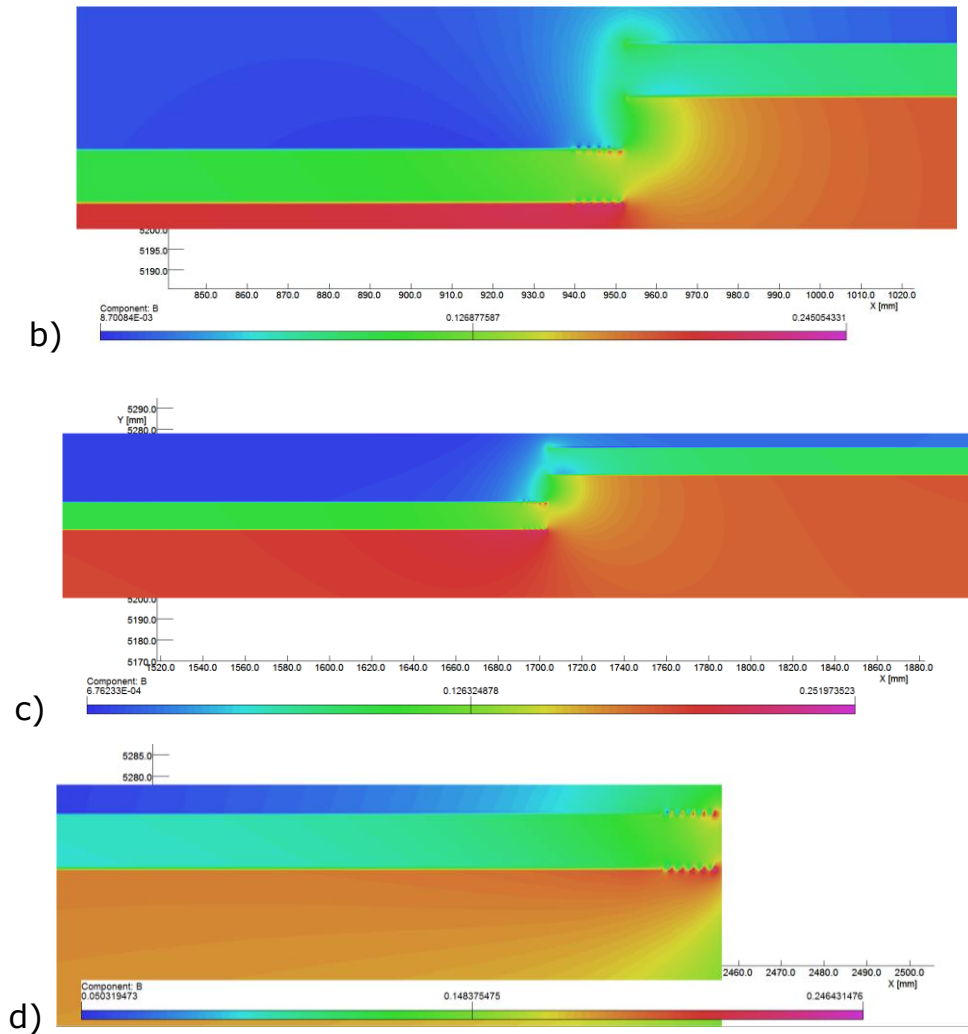


Fig. 21: a) Global view of the field map on the conductor zone. B) Zoom in the detailed geometry conductor. C) Zoom in the first eight superconducting cells.

Fig. 22 is the plot of the field along the X-axis at the altitudes of the different coils' layers. It shows the field enhancement for refined geometry zone with respect to the smeared zone. For instance, the peak field rises from 0.2 T to 0.25 T going from the smeared to the details regions. This coils layer get the highest field. Here again the shielding effect of the adjacent layers is visible with basically half the field for the above upper layer with respect to the lower layers.

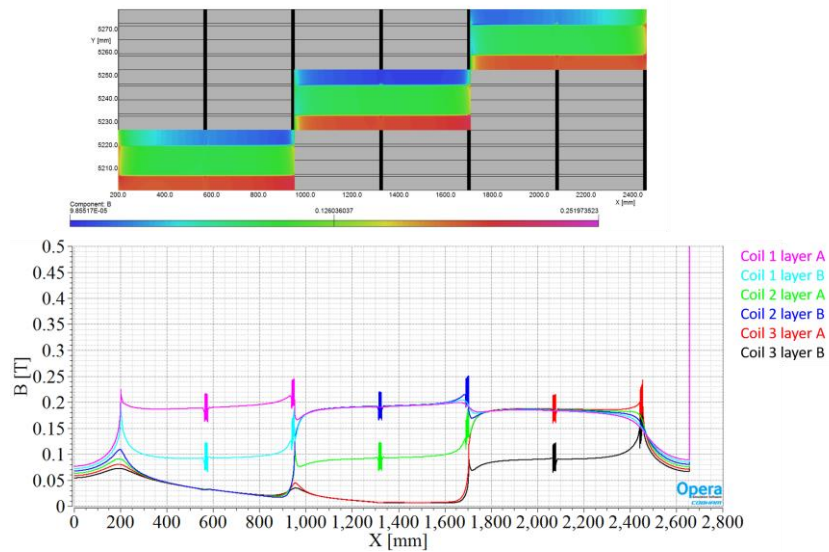


Fig. 22: Plot of the magnetic field along the superconductor for both layers of the tree coils.

3.5 Magnet transfer function computation

Fig. 23 is the plot of the peak field as function of the exciting current obtained from multiple simulations. The linear interpolation ($R^2=1$) is given with a slope of $1.356 \cdot 10^{-3}$ T/kA. The field enhancement computed from 2D model is applied adding an extra 0.05 T to the value computed from 3D model. The inverse of the transfer function gives the magnet load line that is used to determine the magnet performance. We observe that the coil peak field is limited to 0.5 T.

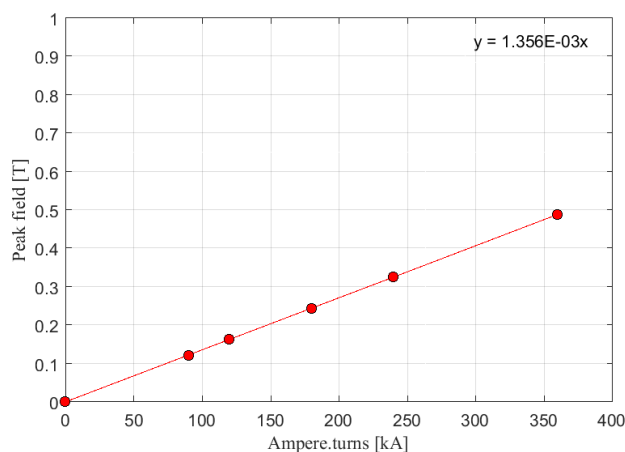


Fig. 23: Magnet transfer function computed combining result from both 2D and 3D models.

3.6 NbTi option

Fig. 24 shows, for the NbTi case, the magnet load-line and the critical currents as function of the field given for both temperatures of 5 and 6 K.

The critical surface is computed using the parameterisation from L. Bottura's fit [6] and reported in the ANNEXE 6.9.1.

The plot indicates the short sample current and field (I_{SS} and B_{SS}) for both temperatures. It allows computing the quench margin as previously defined.

$$\text{Margin @ 6 K} = 100 * \frac{1.245 - 0.5}{1.245} = 60 \%$$

$$\text{Margin @ 5 K} = 100 * \frac{1.625 - 0.5}{1.625} = 69 \%$$

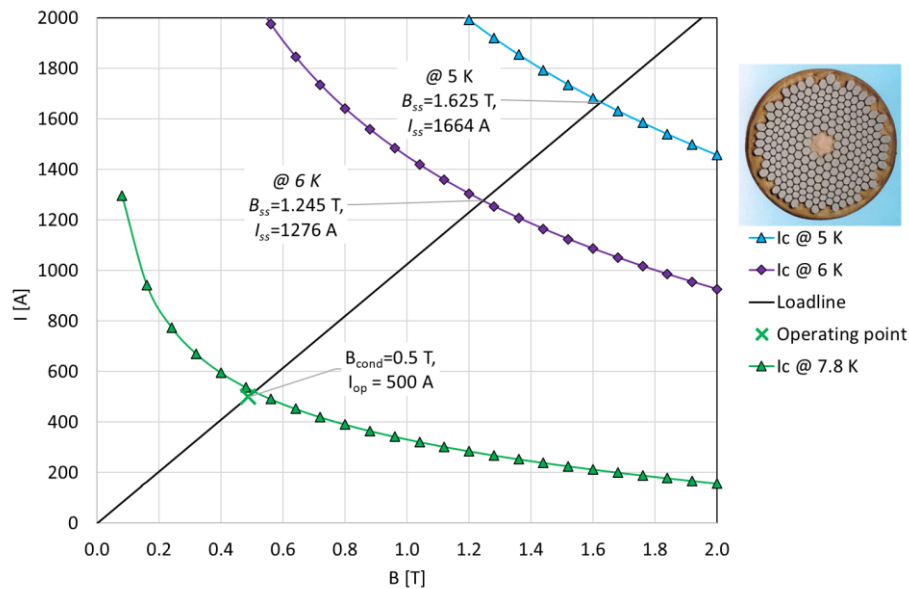


Fig. 24 : LHC MB inner layer NbTi conductor.
Magnet load-line and critical surfaces for two different temperatures: 5 and 6 K.

With a conductor current of 500 A, the required number of turns per coil is 240.

The model gives the total volume of conductor = $3.22 \cdot 10^8 \text{ mm}^3$. With a conductor cross-section of $752 \times 1 \text{ mm}^2$, the total length of conductor is 102 km.

Taking an aspect ratio of 2, 250 micron of turn insulation and an available space for the coil of 750 mm, the rectangular copper stabilizer dimensions are $a = 2.7 \text{ mm}$ and $b = 6 \text{ mm}$. It yields to a copper current density of 30 A/mm^2 . Starting at 6K, the temperature increase by 22.7 K for a hot spot of hot spot is of 28.7 K.

The total conductor weight is 698 kg and the total copper weight is 14298 kg.

3.7 Nb3Sn option

Fig. 25 shows, for the Nb3Sn HL-LHC QXF RRP case, the magnet load-line and the critical current as function of the field given for temperatures of 12 and 14 K.

The critical surface is computed using the parameterisation from L. Godeke's fit [7], [8] and reported in the ANNEXE 6.9.2.

The plot indicates the short sample current and field (I_{ss} and B_{ss}) for both temperatures. It allows computing the quench margin as previously defined.

$$\text{Margin @ 14 K} = 100 * \frac{0.884 - 0.5}{0.884} = 43 \%$$

$$\text{Margin @ 12 K} = 100 * \frac{1.534 - 0.5}{1.534} = 67 \%$$

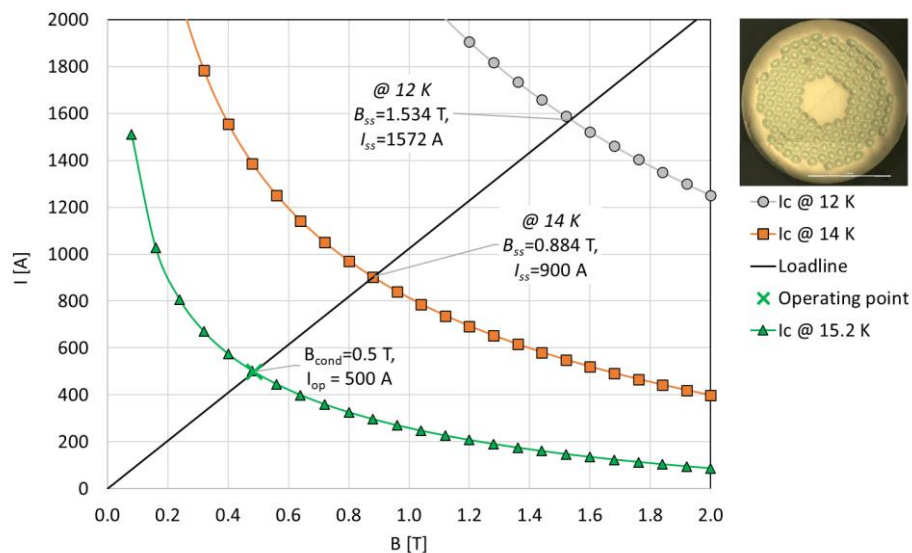


Fig. 25 : HL-LHC QXF RRP Nb₃Sn conductor.
Magnet load-line and critical surfaces for two different temperatures 12 and 14 K.

With a conductor current of 500 A, the required number of turns per coil is then 240.

The model gives the total volume of conductor = $3.22 \cdot 10^8 \text{ mm}^3$. With a conductor cross-section of $752 \times 1 \text{ mm}^2$, the total length of conductor is 102 km.

Taking an aspect ratio of 2.2, 250 micron of turn insulation and an available space for the coil of 752 mm, the rectangular copper stabilizer dimensions are $a = 2.71 \text{ mm}$ and $b = 6 \text{ mm}$. It yields to a copper current density of 30 A/mm^2 . Starting at 12 K, the temperature increase by 24.1 K for a hot spot of 36.1 K.

The total conductor weight is 417 kg and the total copper weight is 14515 kg.

3.8 MgB2 option

Fig. 26 shows, for the MgB₂ HL-LHC Superconducting link round conductor case, the magnet load-line and the critical current as function of the field given for temperatures of 15 and 20 K.

There is so far no published parameterization of the critical current density for MgB₂. The available data are from measurement from Columbus Superconductor [9], [10]. For this study, the focus is made on two different wires. The first get a round cross-section of 1.0 mm diameter and the second a flat cross-section of 3x0.5 mm [11].

The plot indicates the short sample current and field (I_{SS} and B_{SS}) for both temperatures. It allows computing the quench margin as previously defined.

$$\text{Margin @ 20 K} = 100 * \frac{0.88-0.5}{0.88} = 43 \%$$

$$\text{Margin @ 15 K} = 100 * \frac{1.04-0.5}{1.04} = 52 \%$$

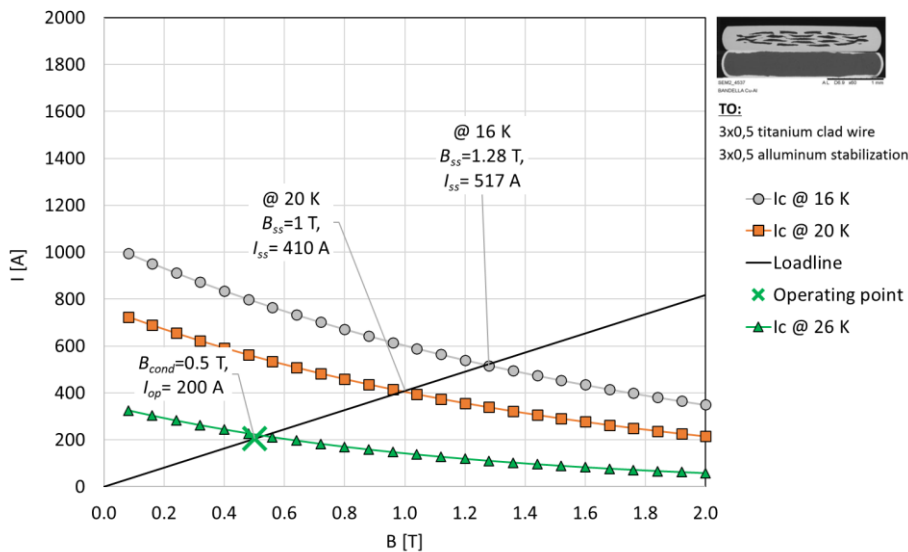


Fig. 26 : HL-LHC Superconducting link MgB₂ round conductor. Magnet load-line and critical surfaces for two different temperatures 15 and 20 K.

With a conductor current of 200 A, the required number of turns per coil is then 600.

The model gives the total volume of conductor = $3.22 \cdot 10^8 \text{ mm}^3$. With a conductor cross-section of $752 \times 1 \text{ mm}^2$, the total length of conductor is 128 km.

For the round wire, taking an aspect ratio of 3.2, 250 micron of turn insulation and an available space for the coil of 752 mm, the rectangular copper stabilizer dimensions are $a = 0.73 \text{ mm}$ and $b = 6.13 \text{ mm}$.

It yields to a copper current density of 12 A/mm². Starting at 20 K, the temperature increase by 9.2 K for a hot spot of 29.2 K.

The total conductor weight is 647 kg and the total copper weight is 8358 kg.

Fig. 27 shows, for the MgB₂ flat conductor case the magnet load-line and the critical current as function of the field given for temperatures of 16 and 20 K.

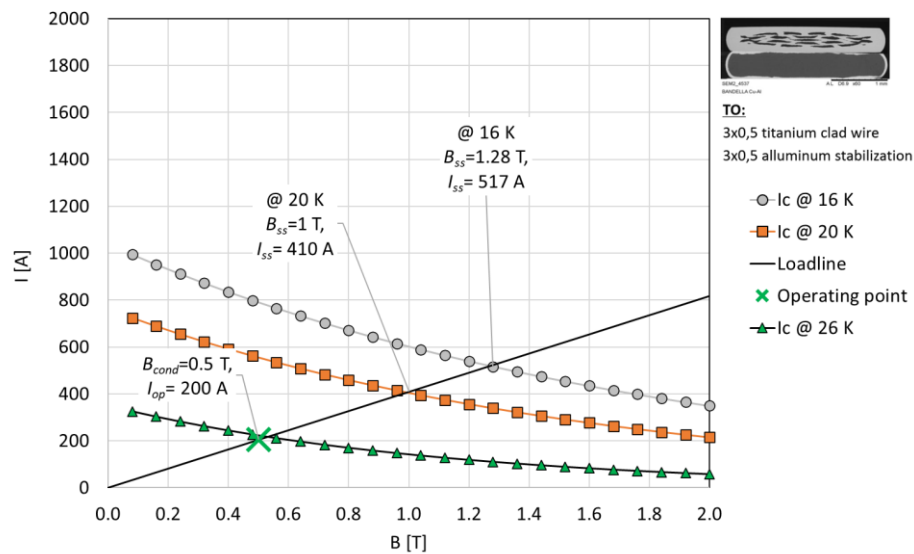


Fig. 27 : Columbus MRI MgB₂ flat conductor. Magnet load-line and critical surfaces for two different temperatures 16 and 20 K.

For the flat conductor, the margins are:

$$\text{Margin @ 20 K} = 100 * \frac{1-0.5}{1} = 50 \%$$

$$\text{Margin @ 16 K} = 100 * \frac{1.28-0.5}{1.28} = 61 \%$$

The model gives the total volume of conductor= 3.22 10⁸ mm³. With a conductor cross-section of 752x1 mm², the total length of conductor is 128 km.

For the flat wire, a= 2.25 mm and b=6.98 mm, the conductor and copper weight are respectively 1237 and 17508 kg.

It yields to a copper current density of 12 A/mm² which produces the same hot spot temperature as for the round wire.

3.9 ReBCO option

Fig. 28 shows, for the ReBCO Fujikura tape, the magnet load-line and the critical current as function of the field given for temperatures of 40 and 50 K.

The critical surface is computed using the parameterisation from [12] and reported in the ANNEXES 0.

The tape is 12 mm wide with a film thickness of 2 μm.

The plot indicates the short sample current and field (I_{SS} and B_{SS}) for both temperatures. It allows computing the quench margin as previously defined.

$$\text{Margin @ 50 K} = 100 * \frac{0.85-0.5}{0.85} = 41 \%$$

$$\text{Margin @ 40 K} = 100 * \frac{1.125-0.5}{1.125} = 56 \%$$

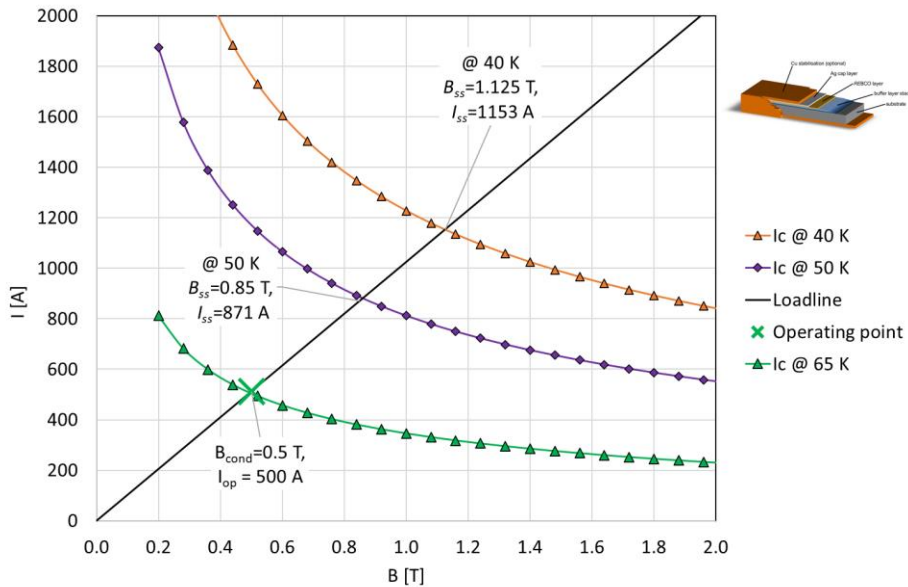


Fig. 28 : Fujikura ReBCO tape conductor.
Magnet load-line and critical surfaces for two different temperatures 50 and 55 K.

With a conductor current of 500 A, the required number of turns per coil is then 240. The model gives the total volume of conductor = $3.22 \cdot 10^8 \text{ mm}^3$. With a conductor cross-section of $752 \times 1 \text{ mm}^2$, the total length of conductor is 128 km. Taking an aspect ratio of 2, 250 micron of turn insulation and an available space for the coil of 752 mm, the rectangular copper stabilizer dimensions are $a = 2.89 \text{ mm}$ and $b = 5.77 \text{ mm}$.

It yields to a copper current density of 30 A/mm^2 . Starting at 50 K, the temperature increases by 6.1 K for a hot spot of 56.1 K

The total conductor weight is 1951 kg and the total copper weight is 22272 kg.

3.10 Superconducting option summary

Fig. 29 compared the various options in terms of quench current margin. All materials can work with conformable margin of more than 40 %.

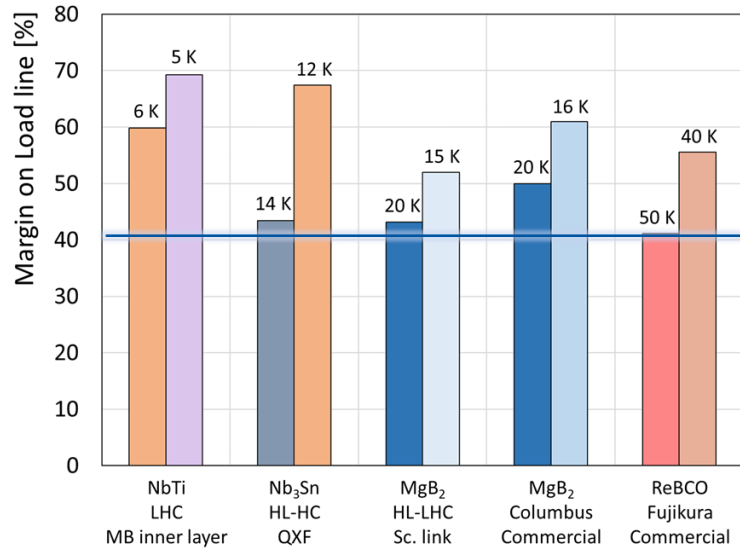


Fig. 29 : Comparison of the margin for NbTi, Nb₃Sn, MgB₂ and ReBCO conductors. The operating temperatures with or without margin are given for each case.

The temperature margin is defined as the difference between operating temperature and the temperature for which the material goes resistive keeping nominal current. This later temperature is just the indicated in green color in the former I-B curve. Fig. 30 compared the options in terms of temperature margin. The MgB₂ and the ReBCO conductor offer large stability facing thermal disturbances with more than 5 K of margin to quench.

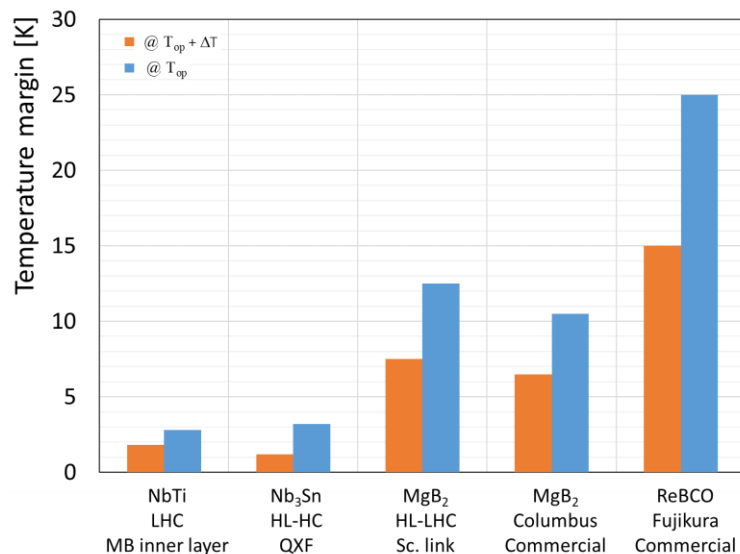


Fig. 30: Comparison of the temperature margin for NbTi, Nb₃Sn, MgB₂ and ReBCO conductors. The operating temperatures with or without margin are given for each case.

Fig. 31, Fig. 32, Fig. 33 and Fig. 34 respectively compares the conductor weight, the copper weight and the corresponding cost for the materials.

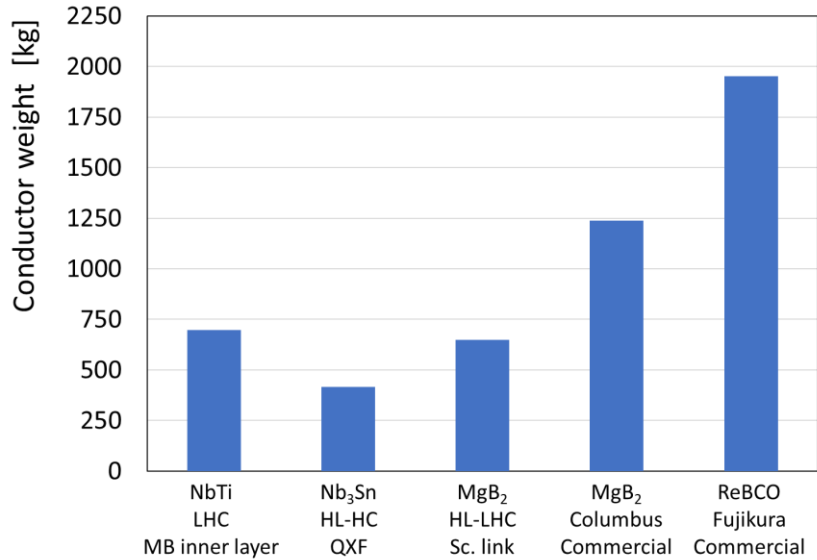


Fig. 31 Comparison of the total weight superconductor for NbTi, Nb₃Sn, MgB₂ and ReBCO cases.

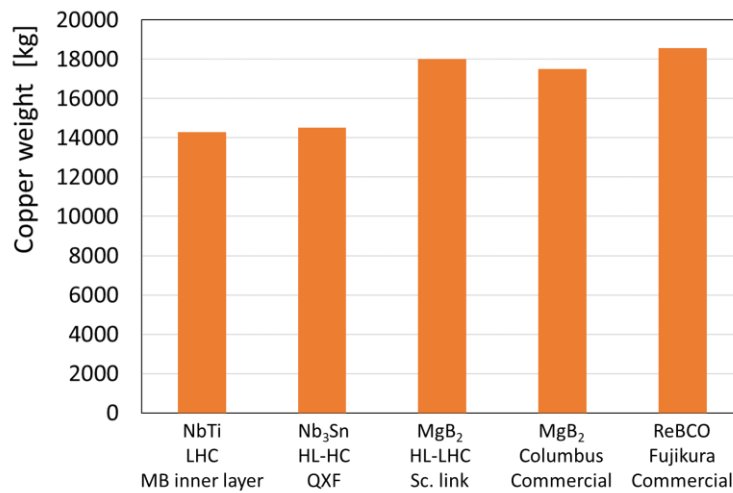


Fig. 32 : Comparison of the amount of copper for NbTi, Nb₃Sn, MgB₂ and ReBCO cases.

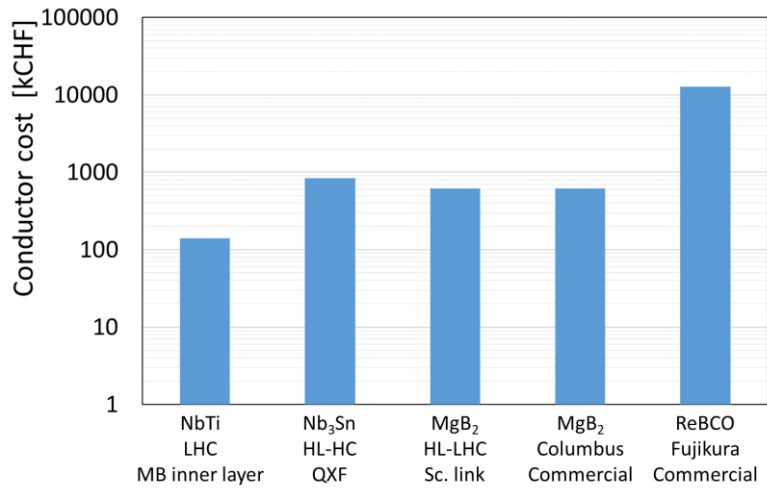


Fig. 33 Comparison of the cost for the superconductor for NbTi, Nb₃Sn, MgB₂ and ReBCO cases.

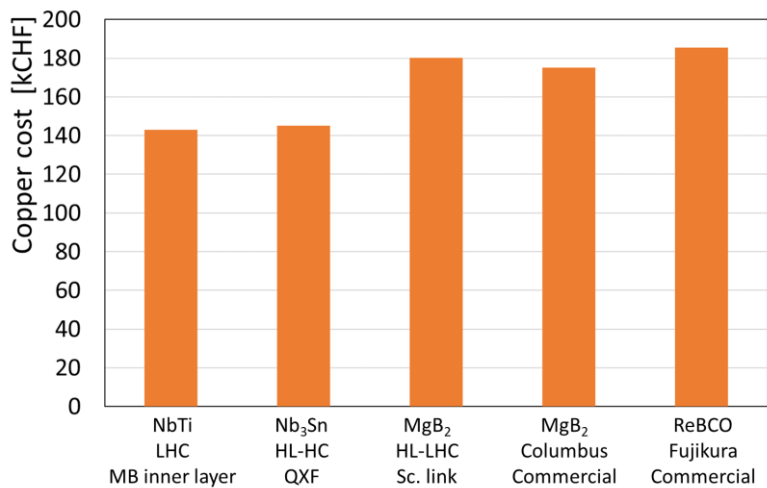


Fig. 34 : Comparison of the cost for copper for NbTi, Nb₃Sn, MgB₂ and ReBCO cases.

The material density and the superconductor costs are indicate in the Table 4 and Table 5 in the ANNEXE 6.10 and 6.11.

Annexe 6.12 reports all the design parameters (operating conditions, conductor cross-section, etc...) used in this report as well as the main results (margin to quench, temperature margin, etc...).

4. Conclusive remark

Different options using either NbTi or Nb₃Sn or MgB₂ or ReBCO have been explored and a comparison made on the operating margins as well as on the cost of the coils have been performed.

All superconducting options are in principle technically feasible. Each of them present advantages and disadvantages:

- NbTi is readily available and cost effective, needs cooling below 6 K
- Nb₃Sn, in this specific magnet, does not represent an interest compared to NbTi or MgB₂.
- MgB₂ can benefit of recent developments, allows operation below 20 K
- ReBCO is expensive and its availability in such long length needs to be explored, however the total amount of conductor needed is relatively small for the coil size and this would allow a simplification of the cryogenic system by operating below 40 K.

The protection to quench can be safely ensured with external dump resistors.

Considering the relatively low peak field induction the MgB₂ option may merit the development of a technical design.

5. Reference

- [1] "Facility to Search for Hidden Particles (ShiP) at the CERN SPS", The ShiP collaboration, CERN-SPSC-2015-016, 8 April 2015.
- [2] "Spectrometer Magnet General design; magnetic field", P. Wertelaers, ShiP vacuum vessel and magnet review, Technical Note, 25 September 2019.
- [3] "Practical Definitions & Formulae for Normal Conducting Magnets", D. Tommasini, Internal Note 2011-18. EDMS 1162401, 2011.
- [4] "ShiP spectrometer magnet, OPERA simulations; Coil cooling design", J. Kurdej, Technical note, 2018.
- [5] "Practical Low Temperature Superconductors for Electromagnets", A. Devred, CERN Scientific Information Service-300-July 2004.
- [6] "A practical Fit for the Critical Surface of NbTi", L. Bottura, IEEE Trans. Appl. Supercond., Vol. 10, No. 1. P. 1054, 2010.
- [7] "Interlaboratory Comparisons of NbTi Critical Current Measurements", A. Godeke et. Al., IEEE Trans. Appl. Supercond., Vol. 19, No. 3. June 2019.
- [8] "Witness sample results for the MQXF short coil #108 (Cable H16OC0216A, HT 336)", B. Bordini et. Al., Internal Note 2018-09, EDMS N: 19878780.
- [9] "Design optimization and evaluation of the 3kA MgB₂ cable at 4.3 K for the superconducting link project at CERN", K Konstantopoulou, J Hurte, P W Retz and A Ballarino, Supercond. Sci. Technol., 32 085003, 2019.
- [10] "The MgB₂ Wire for the Superconducting Link HL-LHC Project", B. Bordini et. Al., International Review of the conceptual Design of the Cold Powering system for the HL-LHC Superconducting Magnets – CERN – 03 July / 04 July 2017.
- [11] "MgB₂ development for magnets in medical application", M. Tropeano, G. Grasso, Superconductivity and other new Developments in Gantry Design for Particle Therapy, September 2015.
- [12] "Parameterization of the critical surface of REBCO conductors from Fujikura", J. Fleiter and A. Ballarino, CERN Internal Note, EDMS 1426239, 2014.
- [13] "Quench detection and diagnostic systems for the superconducting circuits for the HL-LHC", Denz, Reiner (CERN) et. Al., DOI : 10.18429/JACoW-IPAC2019-THPTS036, 2019.
- [14] "Superconducting Magnets", Martin N. Wilson, Oxford Science Publications.

6. Annexe

6.1 Technical drawing for the resistive version

Fig. 35 shows the technical drawing with the various dimension for the resistive version of the SHiP spectrometer magnet.

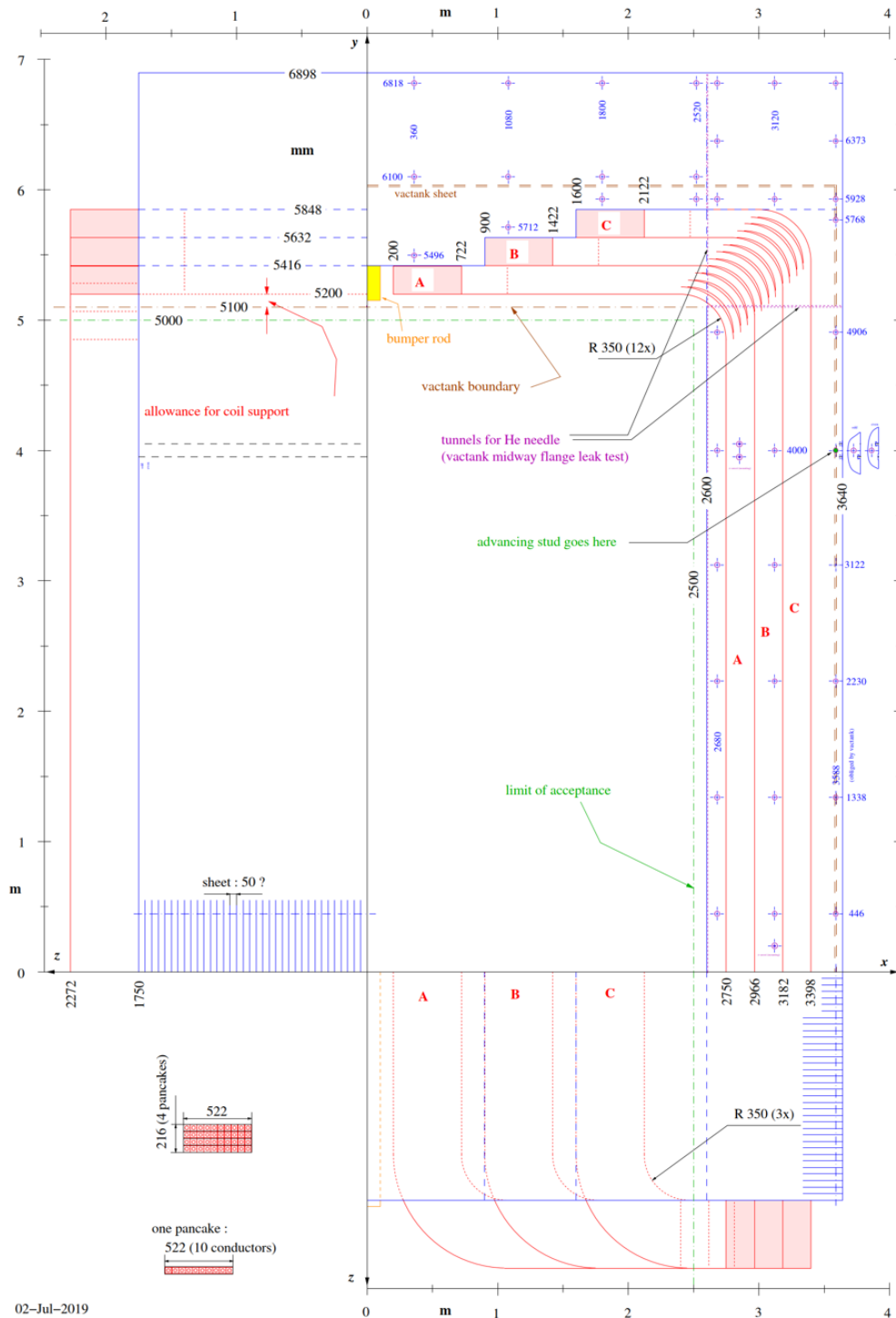


Fig. 35 : Actual geometry of the resistive version of the SHiP spectrometer.

6.2 Coils geometry

Fig. 36 displays the parameters used for the definition of the resistive coils.

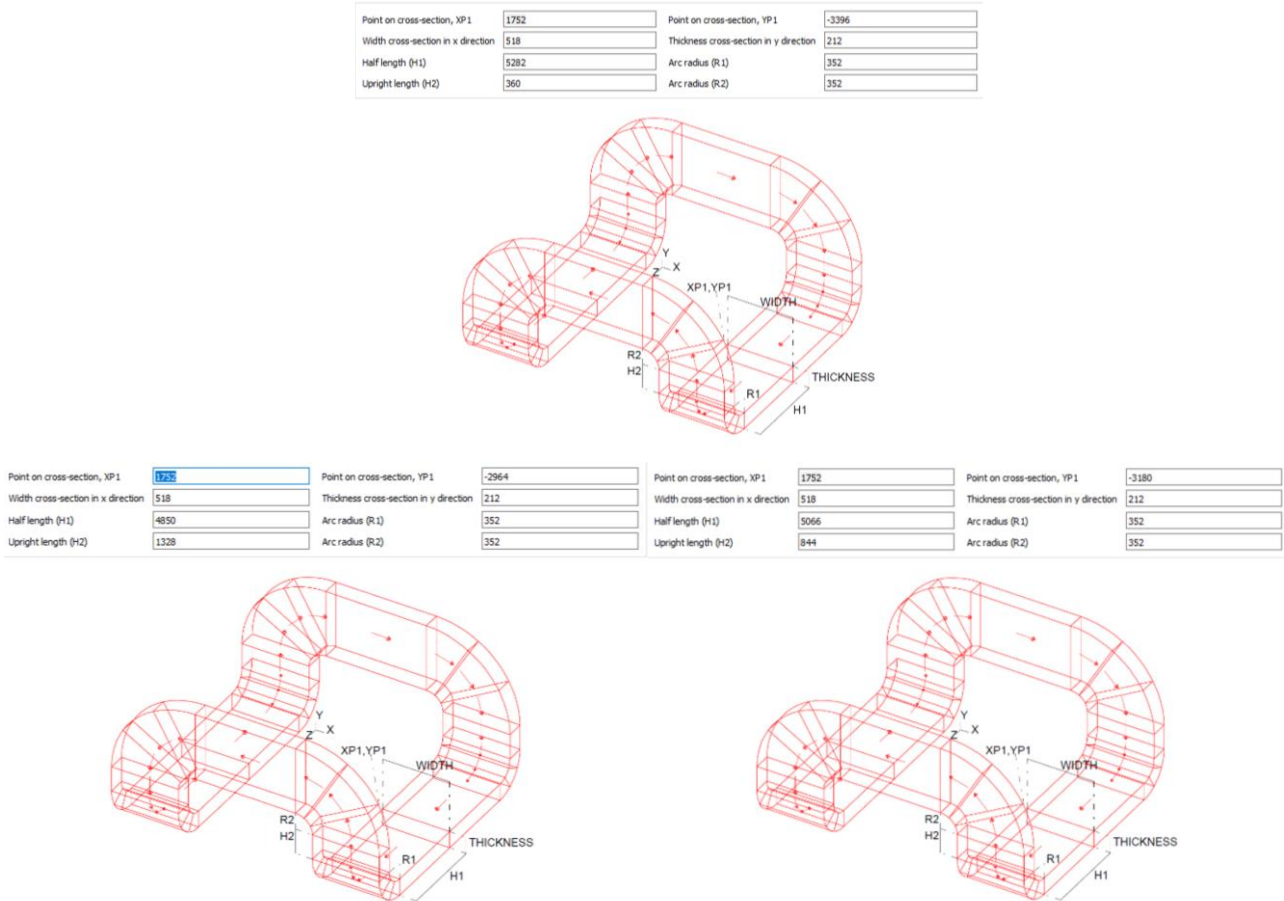


Fig. 36 : Coil dimensions for the resistive version (three coils per pole).

Fig. 37 displays the parameters used for the definition of the superconducting coils.

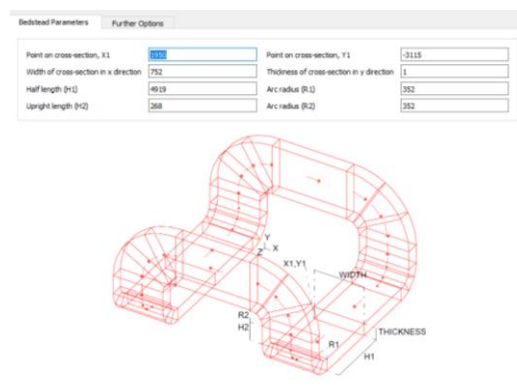


Fig. 37 : Coil dimensions for the superconducting version (three coils per pole).

6.3 Isometric views of the magnet

Fig. 38 displays only the iron yoke and the coils. Fig. 39 a), b) and c) respectively show the front, top and side view of the model.

Fig. 39 d) is a zoom-in the conductor corner showing the space between the coils which is 12 mm. It lets room for the conductor stabilizer and insulation as well as limit the field enhancement due to the proximity of the other coils.

The curvature radius is the same for all corner of the six coils and is 352 mm.

Fig. 37 of ANNEXE 6.2 gives the details of the coil geometry for the six coils.

The iron yoke is 1000 mm thick on the vertical edge and 1500 mm thick for the horizontal edge. 200 mm separates the coils from the iron yoke in order to keep room for the cryostat.

The coil's cross section is $1 \times 752 \text{ mm}^2$ and carries a current density of 80 A/mm^2 .

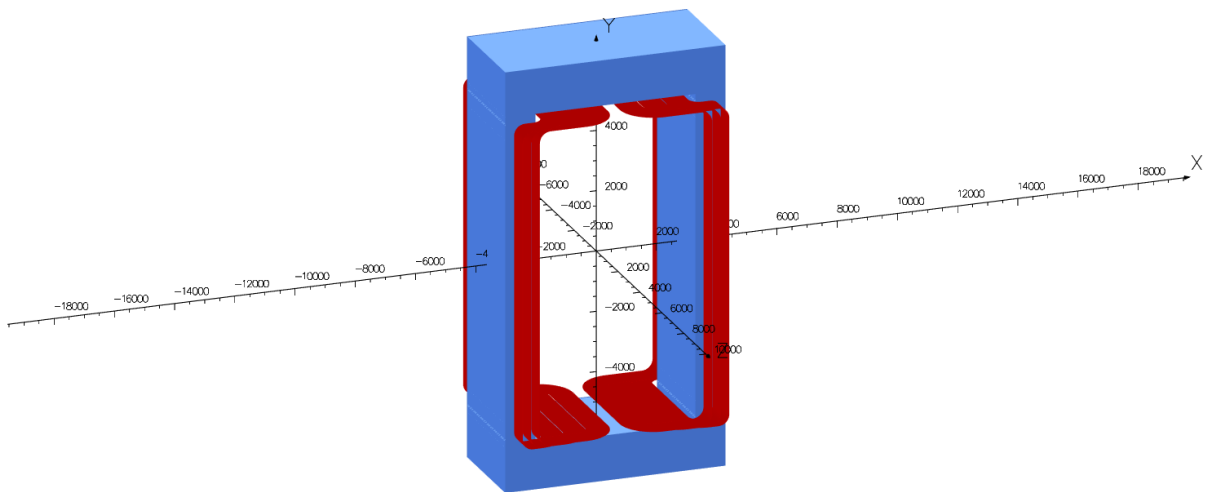
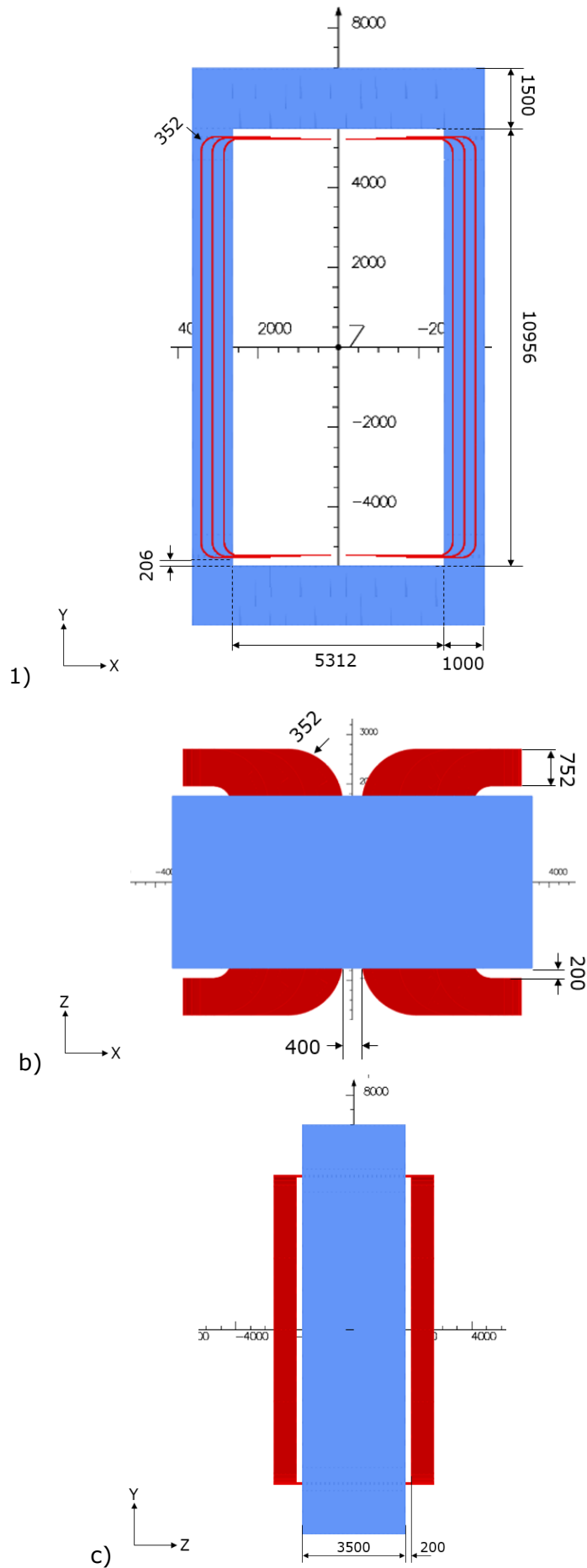


Fig. 38 : Global view of the Opera® 3D model for the superconducting version (without the air region).



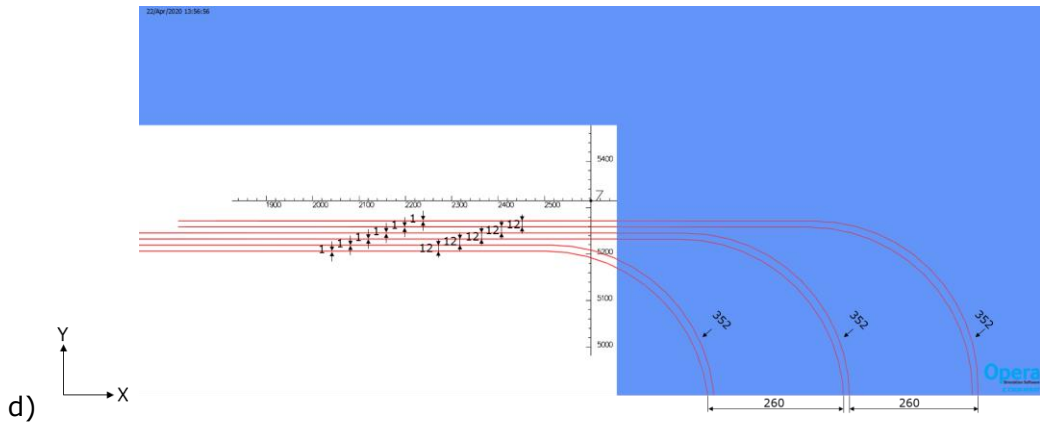


Fig. 39: a) Front, b) top, c) side views of the 3D models and d) zoom in 6 coils.

6.4 View of the 3D mesh

Fig. 40 a) shows the global view of the quadrilateral mesh used for the 3D model. Fig. 40 b), c), d) display the mesh for three different orientations. The mesh is coarser and coarser going away from the conductor with a maximum finite element size of 200 mm. Fig. 41 shows the refined mesh at the vicinity of the conductor with finite element size of 0.25 mm to have four elements on the conductor cross-section.

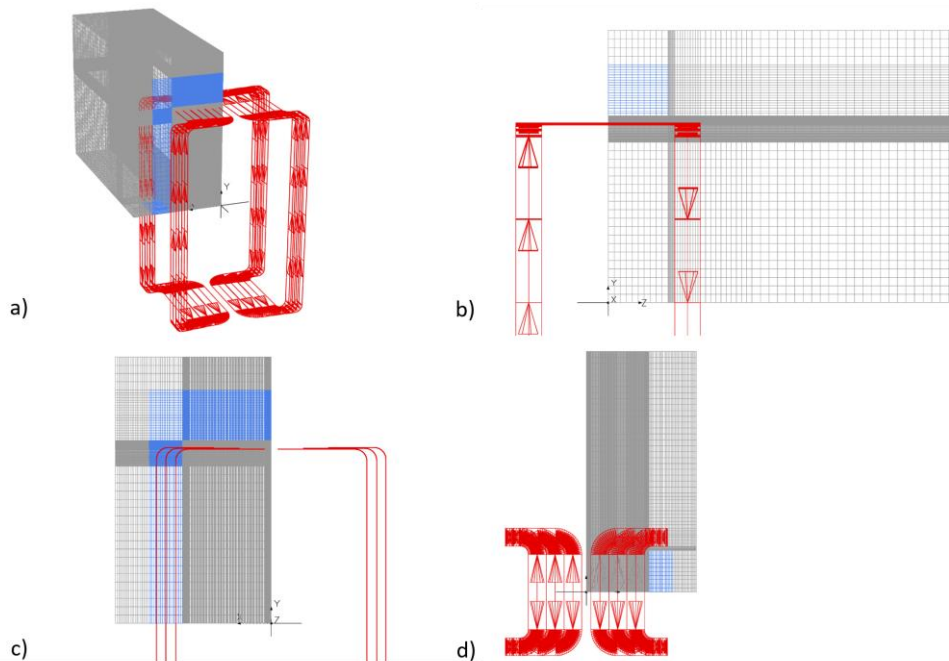


Fig. 40: a) Global view of the mesh, b) Side view of the mesh, c) Front view of the mesh, d) Top view of the mesh.

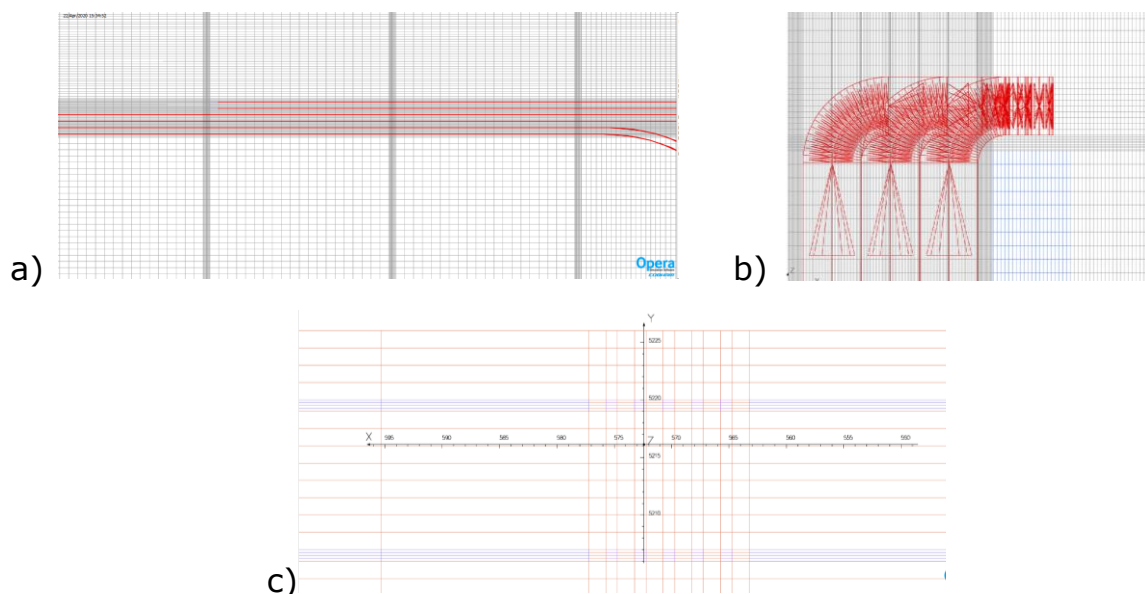


Fig. 41: Zoom-in the refined mesh at the conductor's vicinity. a) front view with mesh density increase, b) top view and c) zoom-in the coil cross-section with 4 FE/mm.

6.5 BH curve for the iron

The plot of the Magnetic Flux Density (B) versus the Magnetic Field Strength (H) is shown in Fig. 42.

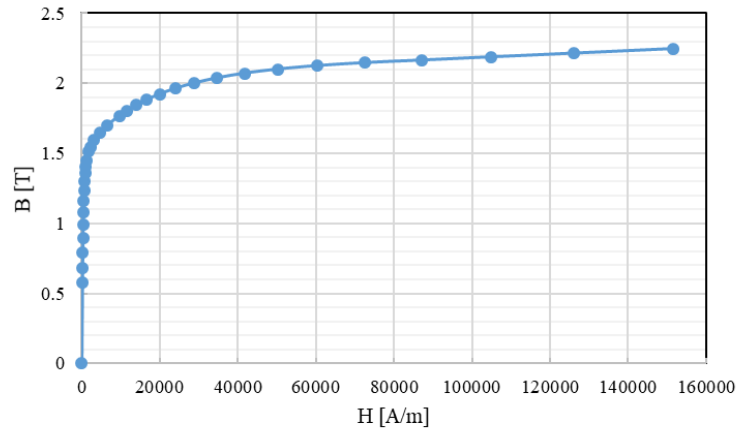


Fig. 42: BH curve used for the iron and referred to "tnten.bh" in the Opera® database.

6.6 View of the 2D mesh

Fig. 43 shows the quadrilateral mesh used for the 2D model with refined mesh at the conductor regions. Fig. 44 displays the finer mesh in the conductor zone with 30 finite elements per mm. The mesh density is then much higher than the one used in the 3D model.

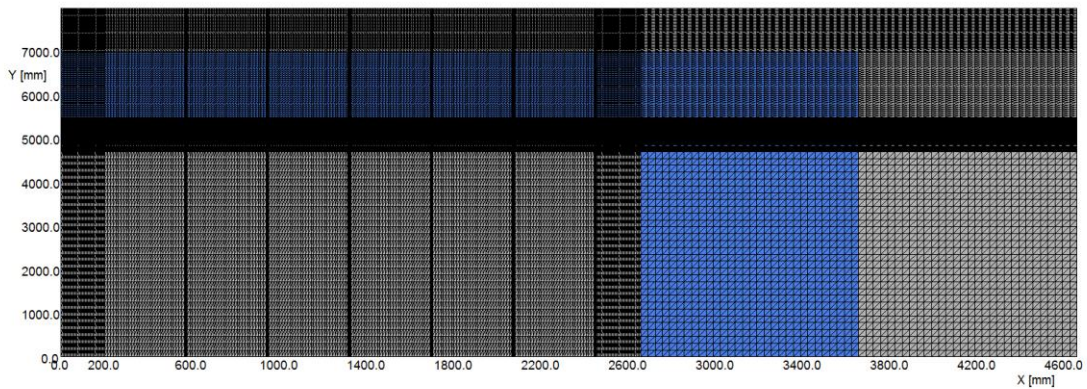


Fig. 43 : Global view of the mesh for the 2D model.

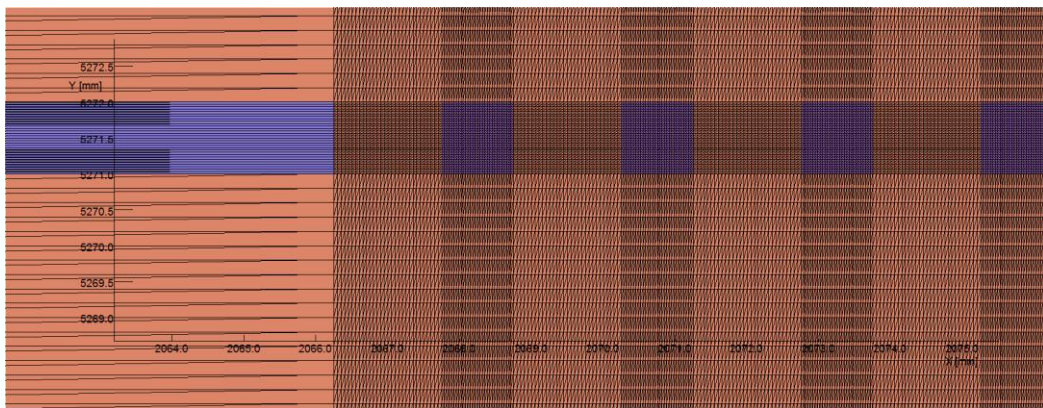


Fig. 44 : Zoom-in the mesh used for the detailed conductor.

6.7 Field lines, field in the acceptance region and in the iron for the 2D model

6.7.1 Field lines

Fig. 45 demonstrates that the field lines effectively respect the applied boundary conditions with normal and tangential fields on the inner side and external sides.

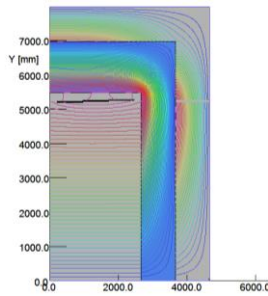


Fig. 45: Plot of the potential lines showing the relevance of the boundary conditions.

6.7.2 Field within the acceptance region

Fig. 46 shows the field map in the area enclosed by the iron yoke. The field is uniform in the magnet aperture with a B_0 0.167 T slightly higher than the 3D model results. The coils tend to shield the field above with almost zero field below the iron.

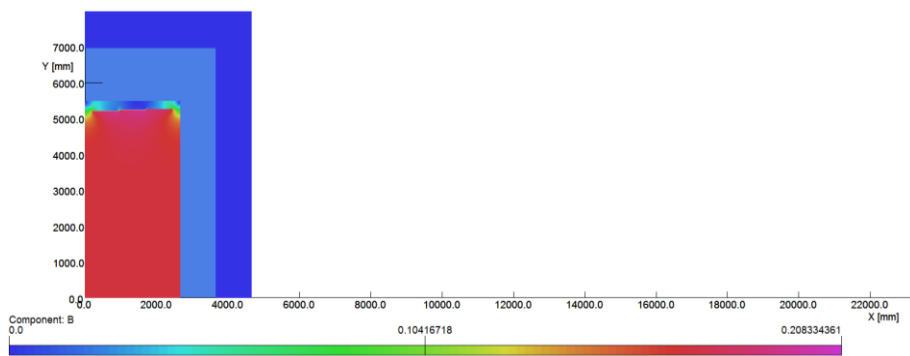


Fig. 46 : Field map for the air region enclosed in the iron yoke with an average field of 0.16 T.

6.7.3 Field in the iron

Fig. 47 shows the field in the iron. The maximum field of 1.48 T is as expected slightly lower than the field computed with the 3D model (1.63 T). The field map also shows that the iron yoke completely shields the magnetic field.

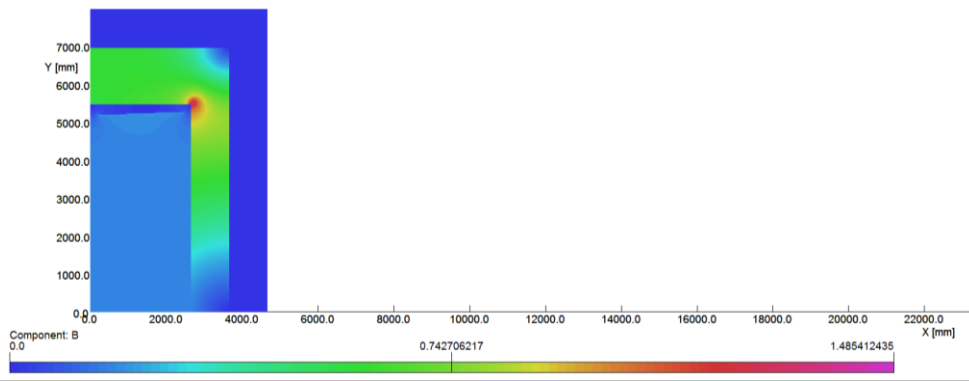


Fig. 47: Field map on the iron showing field concentration at the inner corner with a maximum amplitude of 1.48 T.

6.8 Magnet protection scheme

A dedicated electrical circuit a dump resistor in parallel to the magnet, assuming long energization time (few hours) is shown in Fig. 48.

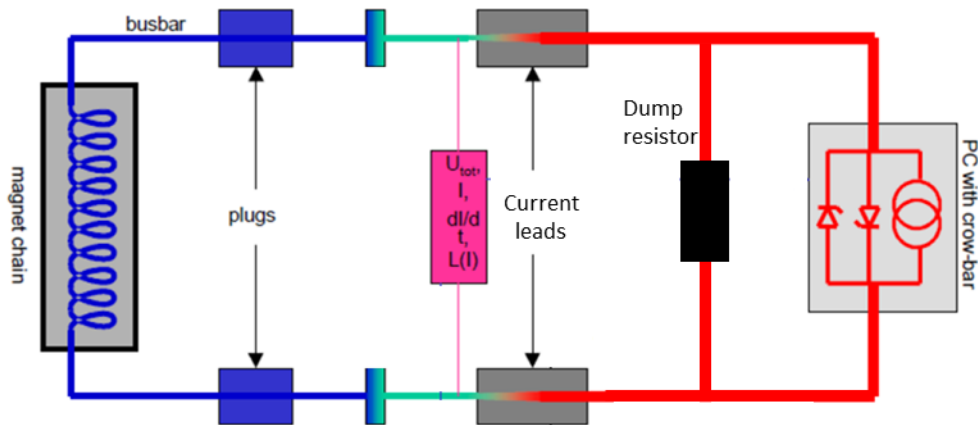


Fig. 48: Electrical circuit featuring the power converter in series with the magnet through current leads and bus bar. The dump resistor is set in parallel to the magnet.

6.9 Critical surface scaling law

6.9.1 NbTi

From L. Bottura's fit [6], the critical current density J_c of typical NbTi strand can be expressed as function of the reduced temperature t and the reduced field b . The relation reads:

$$J_c(B, T) = \frac{C_0}{B} b^\alpha (1 - b)^\beta (1 - t^n)^\gamma$$

With:

$$t = \frac{T}{T_{c0}}$$

$$b = \frac{B}{B_{c2}(T)}$$

With T and B the applied temperature and field, T_{c0} the maximum critical temperature (at $B=0$) and B_{c2} the maximum upper critical field (at $T=0$):

$$B_{c2}(T) = B_{c20}(1 - t^n)$$

Table 1 gives the parameters for the fit relative to the LHC MB strand

Table 1 : Critical current density Bottura's fit parameters.

	LHC MB	Units
B_{c20}	14.5	[T]
T_{c0}	9.2	[K]
C_0	27.04	[T]
a	0.57	[-]
b	0.9	[-]
g	2.32	[-]
n	1.7	[-]

With this set of parameters, the critical current I_c is defined as the product of the critical current density multiplied by cross-section of the strand:

$$I_c = J_c * A_{strand}$$

$$A_{strand} = \pi \frac{D_{strand}^2}{4}$$

A cross-check can be made on the typical measured value at 4.2 K and 5 T from [7] of 536 A for the outer layer strand:

$$I_c(4.2 K, 5 T) = 518 [A]$$

6.9.2 Nb₃Sn

From L. Godeke's fit [8], the critical current density J_c of typical Nb₃Sn strand can be expressed as function of the reduced temperature t , the reduced field b and the deviatoric strain function $s(\varepsilon)$. The relation reads:

$$J_c(B, T, \varepsilon) = \frac{C_1}{B} s(\varepsilon) (1 - t^n)^\gamma (1 - t^2) b^\alpha (1 - b)^\beta$$

With:

$$t = \frac{T}{T_{cm}^*(\varepsilon)}$$

$$b = \frac{B}{B_{c2}(T, \varepsilon)}$$

$$B_{c2}(T) = B_{c20} s(\varepsilon) (1 - t^n)$$

$$T_{cm}^* = T_{cm} s(\varepsilon)^{1/3}$$

$$s(\varepsilon) = \frac{C_{a1} \left[\sqrt{(\varepsilon_{shift})^2 + (\varepsilon_{0,a})^2} - \sqrt{(\varepsilon_{axial} - \varepsilon_{shift})^2 + (\varepsilon_{0,a})^2} \right] - C_{a2} \varepsilon_{axial}}{1 - C_{a1} \varepsilon_{0,a}} + 1$$

$$\varepsilon_{axial} = \varepsilon_{applied} + \varepsilon_m$$

With T and B the applied temperature and field, T_{c0} the maximum critical temperature (at $B=0$) and B_{c2} the maximum upper critical field (at $T=0$).

The strain is set to zero in the present analysis but should be adapted later on to get a more accurate evaluation of the critical current.

Table 2 gives the parameters for the fit relative to the HL-LHC QXF strands [8].

Table 2 : Critical current density Godeke's fit parameters.

	HL-LHC QXF	Units
B_{c20}	27.65	[T]
T_{c0}	16.95	[K]
C_1	216.2	[kAT/mm ²]
C_{a1}	47.6	[T]
C_{a2}	6.43	[T]
$\varepsilon_{0,a}$	0.273	[%]
$\varepsilon_{m,SHIP}$	0	[%]
ε_{shift}	0.037	[%]
$\varepsilon_{applied}$	0	[%]
ε_{axial}	0	[%]
a	0.5	[-]
b	2	[-]
g	1.37	[-]
n	1.52	[-]

With this set of parameters, the critical current I_c is defined as the product of the critical current density multiplied by cross-section of the strand relative to the non-copper part, α_{Cu-nCu} :

$$I_c = J_c * A_{sc}$$

$$A_{sc} = \frac{A_{strand}}{\alpha_{Cu-nCu} + 1}$$

A crosscheck on the typical measured value at 4.2 K and 12 T from [8] of 650 A for the HL-LHC strand gives:

$$I_c(4.2 K, 12 T) = 675 [A]$$

6.9.3 MgB₂

There is so far no published parameterization of the critical current density for MgB₂. The available data are from measurement from Columbus Superconductor [10]. Different MgB₂ wires have been tested as function of the temperature and field. For this study, the focus is made on two different wires. The first get a round cross-section of 1.5 mm diameter and the second a flat cross-section of 3x0.5 mm. The first is intended to be used in the HL-LHC superconducting link [9] and the second dedicated to MRI medical application [11].

6.9.4 ReBCO

From J. Fleiter's fit [12], the critical current density J_c of typical ReBCO tape can be expressed as function of the reduced temperature t , the reduced field b and the angular dependence g . The relations for perpendicular and parallel field respectively read:

$$J_{c,c} = \frac{\alpha_c}{B} b_c^{p_c} (1 - b_c)^{q_c} (1 - t^n)^{\gamma_c}$$

$$J_{c,ab} = \frac{\alpha_{ab}}{B} b_{ab}^{p_{ab}} (1 - b_{ab})^{q_{ab}} [(1 - t^{n_1})^{n_2} + a (1 - t^n)]^{\gamma_{ab}}$$

Where:

$$b_{ab} = B/B_{i,ab}, b_c = B/B_{i,c}, t = T/T_{c0}$$

$$B_{i,ab} = B_{i0,ab} \left((1 - t^{n_1})^{n_2} + a (1 - t^n) \right)$$

$$B_{i,c} = B_{i0,c} (1 - t^n)$$

Adding the fit of angular dependence θ , the critical current density is:

$$J_c(B, T, \theta) = J_{c,c}(B, T) + \frac{J_{c,ab}(B, T) - J_{c,c}(B, T)}{1 + \left(\frac{\theta - \pi/2}{g(B, T)} \right)^v}$$

$$g(B, T) = g_0 + g_1 \exp(-[g_2 \exp(g_3 T)]B)$$

Table 3 : Critical current density Fleiter's fit parameters.

	Fujikura	Units
g_0	0.03	[-]
g_1	0.25	[-]
g_2	0.06	[-]
g_3	0.058	[-]
T_{c0}	93	[K]
p_c	0.5	[-]
q_c	2.5	[-]
$B_{i0,c}$	140	[T]
γ_c	2.44	[-]
α_c	1.86	[MA T/mm ²]
n	1	[-]
n_1	1.4	[-]
n_2	4.45	[-]
p_{ab}	1	[-]
q_{ab}	5	[-]
$B_{i0,ab}$	250	[T]
a	0.1	[-]
γ_{ab}	1.63	[-]
α_{ab}	68.3	[MA T/mm ²]
thickness	0.002	[mm]

width	12	[mm]
-------	----	------

6.10 Material density

Table 4 : Material density.

Copper	8960	kg/m ³
NbTi	6000	kg/m ³
Nb ₃ Sn	5400	kg/m ³
MgB ₂	2600	kg/m ³
ReBCO	6350	kg/m ³

6.11 Conductor price

Table 5 : Conductor price

Copper	10	CHF/kg
NbTi	200	CHF/kg
Nb ₃ Sn	2000	CHF/kg
MgB ₂	4.8	CHF/m
ReBCO	100	CHF/m

6.12 Summary tables for the superconducting options

Table 6 gives for the different materials, the operating temperatures (T_{op}), field (B_{op}) and current (I_{op}), the total number of turns (N_{total}), the magnet current (I_{magnet}), the conductor peak field (B_{cond}), the short sample limits (field and current) for both temperature (I_{ss} and B_{ss}).

It also gives the quench margin and the temperature margins. The strand area and copper non-copper ratio are reported as well.

Table 6 : Summary of the design parameters for the SHIP superconducting options.

T_{op} [K]	B_{gap} [T]	I_{op} [A]	N_{total} [-]	I_{magnet} [A]	B_{cond} [T]	I_{ss} [A]	B_{ss} [T]	B Margin [%]	T Margin [K]	S_{strand} [mm ²]	Cu-ncu [-]
6	0.15	500	1440	720000	0.5	1276	1.245	60	1.8	0.891	1.65
5	0.15	500	1440	720000	0.5	1664	1.625	69	2.8	0.89	1.65
Nb₃Sn RRP QXF											
T_{op} [K]	B_{gap} [T]	I_{op} [A]	N_{total} [-]	I_{magnet} [A]	B_{cond} [T]	I_{ss} [A]	B_{ss} [T]	B Margin [%]	T Margin [K]	S_{strand} [mm ²]	Cu-ncu [-]
14	0.15	500	1440	720000	0.5	900	0.884	43	1.2	0.567	1.20
12	0.15	500	1440	720000	0.5	1572	1.534	67	3.2	0.567	1.20
MgB₂ 1.0 mm Round wire											
T_{op} [K]	B_{gap} [T]	I_{op} [A]	N_{total} [-]	I_{magnet} [A]	B_{cond} [T]	I_{ss} [A]	B_{ss} [T]	B Margin [%]	T Margin [K]	S_{strand} [mm ²]	Cu-ncu [-]
20	0.15	200	3600	720000	0.5	343	0.88	43	8	0.79	1.70
15	0.15	200	3600	720000	0.5	413	1.04	52	13	0.79	1.70
MgB₂ 3x0.5 mm flat wire											
T_{op} [K]	B_{gap} [T]	I_{op} [A]	N_{total} [-]	I_{magnet} [A]	B_{cond} [T]	I_{ss} [A]	B_{ss} [T]	B Margin [%]	T Margin [K]	S_{strand} [mm ²]	Cu-ncu [-]
20	0.15	200	3600	720000	0.5	410	1	50	7	1.50	1.70
16	0.15	200	3600	720000	0.5	517	1.28	61	11	1.50	1.70
ReBCO 0.2x12 mm tape											
T_{op} [K]	B_{gap} [T]	I_{op} [A]	N_{total} [-]	I_{magnet} [A]	B_{cond} [T]	I_{ss} [A]	B_{ss} [T]	B Margin [%]	T Margin [K]	S_{strand} [mm ²]	Cu-ncu [-]
50	0.15	500	1440	720000	0.5	871	0.85	41	15	2.40	0.00
40	0.15	500	1440	720000	0.5	1153	1.125	56	25	2.40	0.00

Table 7 gives together with the material reference and the operating conditions, copper cross section for the strand itself ($S_{Cu, strand}$), the current density in the copper ($J_{Cu max}$), the corresponding stabilizer area (S_{stab}) with the thickness and width (a_{stab} , b_{stab}). It gives also the total length of stabilized conductor (l_{cond}), the weight of the superconducting material (m_{sc}) and of the copper stabilizer (m_{Cu}) and their relative costs.

Table 7 : Summary of the design parameters for the ShiP superconducting options.
Parameter relative to the conductor cross-section

NbTi LHC MB Inner layer													
T_{op}	I_{op}	$S_{Cu,strand}$	$J_{Cu max}$	$S_{Cu,tot}$	S_{stab}	a_{stab}	b_{stab}	l_{cond}	m_{sc}	m_{Cu}	Conductor cost	Copper cost	
[K]	[A]	[mm ²]	[A/mm ²]	[mm ²]	[mm ²]	[mm]	[mm]	[km]	[kg]	[kg]	[kCHF]	[kCHF]	
6	500	0.55	30	16.7	16.1	5.98	2.69	102	698	14298	140	143	
5	500	0.55	30	16.7	16.1	5.98	2.69	102	698	14298	140	143	
Nb₃Sn RRP QXF													
T_{op}	I_{op}	$S_{Cu,strand}$	$J_{Cu max}$	$S_{Cu,tot}$	S_{stab}	a_{stab}	b_{stab}	l_{cond}	m_{sc}	m_{Cu}	Conductor cost	Copper cost	
[K]	[A]	[mm ²]	[A/mm ²]	[mm ²]	[mm ²]	[mm]	[mm]	[km]	[kg]	[kg]	[kCHF]	[kCHF]	
14	500	0.31	30	16.7	16.4	6.03	2.71	102	417	14515	833	145	
12	500	0.31	30	16.7	16.4	6.03	2.71	102	417	14515	833	145	
MgB₂ 1.0 mm Round wire													
T_{op}	I_{op}	$S_{Cu,strand}$	$J_{Cu max}$	$S_{Cu,tot}$	S_{stab}	a_{stab}	b_{stab}	l_{cond}	m_{sc}	m_{Cu}	Conductor cost	Copper cost	
[K]	[A]	[mm ²]	[A/mm ²]	[mm ²]	[mm ²]	[mm]	[mm]	[km]	[kg]	[kg]	[kCHF]	[kCHF]	
20	200	0.49	12	16.7	16.2	2.25	7.19	128	647	18009	614	180	
15	200	0.49	12	16.7	16.2	2.25	7.19	128	647	18009	614	180	
MgB₂ 3x0.5 mm flat wire													
T_{op}	I_{op}	$S_{Cu,strand}$	$J_{Cu max}$	$S_{Cu,tot}$	S_{stab}	a_{stab}	b_{stab}	l_{cond}	m_{sc}	m_{Cu}	Conductor cost	Copper cost	
[K]	[A]	[mm ²]	[A/mm ²]	[mm ²]	[mm ²]	[mm]	[mm]	[km]	[kg]	[kg]	[kCHF]	[kCHF]	
20	200	0.94	12	16.7	15.7	2.25	6.98	128	1237	17508	614	175	
16	200	0.94	12	16.7	15.7	2.25	6.98	128	1237	17508	614	175	
ReBCO 0.2x12 mm tape													
T_{op}	I_{op}	$S_{Cu,strand}$	$J_{Cu max}$	$S_{Cu,tot}$	S_{stab}	a_{stab}	b_{stab}	l_{cond}	m_{sc}	m_{Cu}	Conductor cost	Copper cost	
[K]	[A]	[mm ²]	[A/mm ²]	[mm ²]	[mm ²]	[mm]	[mm]	[km]	[kg]	[kg]	[kCHF]	[kCHF]	
50	500	0.00	30	16.7	16.7	5.77	2.89	128	1951	18560	12800	186	
40	500	0.00	30	16.7	16.7	5.77	2.89	128	1951	18560	12800	186	



The SHiP spectrometer magnet – Superconducting options

Hugues Bajas, Davide Tommasini

CERN

Abstract

This document describes a study of the choice of conductor and its design for the SHiP spectrometer.

The SHiP spectrometer magnet – Superconducting options

Table 8 gives, together from the material and operating conditions: the magnet inductance (L), the maximum allowable voltage (U_{\max}), the dump resistor value (R_{dump}), the time constant of the current discharge during energy extraction (τ), the quench integral and the corresponding hot spot temperature (T_{HotSpot}).

Table 8 : Summary of the design parameters for the ShiP superconducting options. Parameter relative to the magnet protection.

NbTi LHC MB Inner layer							
T_{op}	I_{op}	L	U_{\max}	R_{dump}	τ	QI	$T_{\text{Hot Spot}}$
[K]	[A]	[H]	[V]	[Ω]	[s]	[$\text{MA}^2 \cdot \text{s}$]	[K]
6	500	43	1000	2.0	22	2.7	30
5	500	43	1000	2.0	22	2.7	29
Nb₃Sn RRP QXF							
T_{op}	I_{op}	L	U_{\max}	R_{dump}	τ	QI	$T_{\text{Hot Spot}}$
[K]	[A]	[H]	[V]	[Ω]	[s]	[$\text{MA}^2 \cdot \text{s}$]	[K]
14	500	43	1000	2.0	22	2.7	36.1
12	500	43	1000	2.0	22	2.7	34.1
MgB₂ 1.0 mm Round wire							
T_{op}	I_{op}	L	U_{\max}	R_{dump}	τ	QI	$T_{\text{Hot Spot}}$
[K]	[A]	[H]	[V]	[Ω]	[s]	[$\text{MA}^2 \cdot \text{s}$]	[K]
20	200	229	1000	5.0	46	0.9	29.2
15	200	229	1000	5.0	46	0.9	24.2
MgB₂ 3x0.5 mm flat wire							
T_{op}	I_{op}	L	U_{\max}	R_{dump}	τ	QI	$T_{\text{Hot Spot}}$
[K]	[A]	[H]	[V]	[Ω]	[s]	[$\text{MA}^2 \cdot \text{s}$]	[K]
20	200	229	1000	5.0	46	0.9	29.2
16	200	229	1000	5.0	46	0.9	25.2
ReBCO 0.2x12 mm tape							
T_{op}	I_{op}	L	U_{\max}	R_{dump}	τ	QI	$T_{\text{Hot Spot}}$
[K]	[A]	[H]	[V]	[Ω]	[s]	[$\text{MA}^2 \cdot \text{s}$]	[K]
50	500	43	1000	2.0	22	2.7	56.1
40	500	43	1000	2.0	22	2.7	46.1